

# Coupled, Physics-based Modeling Reveals Earthquake Displacements are Critical to the 2018 Palu, Sulawesi Tsunami

T. Ulrich<sup>1</sup>, S. Vater<sup>2</sup>, E. H. Madden<sup>1,3</sup>, J. Behrens<sup>4</sup>, Y. van Dinther<sup>5</sup>, I. van Zelst<sup>6</sup>, E. J. Fielding<sup>7</sup>, C. Liang<sup>8</sup>, and A.-A. Gabriel<sup>1</sup>

ulrich@geophysik.uni-muenchen.de

**Abstract** The September 2018,  $M_w$  7.5 Sulawesi earthquake occurring on the Palu-Koro strike-slip fault system was followed by an unexpected localized tsunami. We show that direct earthquake-induced uplift and subsidence could have sourced the observed tsunami within Palu Bay. To this end, we use a physics-based, coupled earthquake-tsunami modeling framework tightly constrained by observations. Our model combines rupture dynamics, seismic wave propagation, tsunami propagation and inundation. The earthquake scenario, featuring sustained supershear rupture propagation, matches key observed earthquake characteristics, including the moment magnitude, rupture duration, fault plane solution, teleseismic waveforms and inferred horizontal ground displacements. In our model, a straight fault segment dipping  $65^\circ$  East beneath Palu Bay hosts a combination of up to 6 m left-lateral slip and up to 2 m normal slip determined by a regional transtensional stress regime. The time-dependent, 3D seafloor displacements are translated into bathymetry perturbations with a mean vertical offset of 1.5 m across the submarine fault segment. This sources a tsunami with wave amplitudes

and periods that match those measured at the Pantoloan wave gauge and inundation that reproduces observations from field surveys. We conclude that a source related to earthquake displacements is probable and that landsliding may not have been the primary source of the tsunami. Our results have important implications for submarine strike-slip fault systems worldwide. Physics-based modeling offers rapid response specifically in tectonic settings which are currently underrepresented in operational tsunami hazard assessment.

**Keywords** Sulawesi, tsunami, earthquake dynamics, coupled model, physics-based modeling, strike slip

## 1 Introduction

Tsunamis occur due to abrupt perturbations to the water column, usually caused by the seafloor deforming during earthquakes or submarine landslides. Devastating tsunamis associated with submarine strike-slip earthquakes are rare. While such events may trigger landslides that in turn trigger tsunamis, the associated ground displacements are predominantly horizontal, not vertical, which does not favor tsunami genesis.

However, strike-slip fault systems in complex tectonic regions, such as the Palu-Koro fault zone cutting across the island of Sulawesi, may produce vertical deformation. Strike-slip systems may also include complicated fault geometries, such as non-vertical faults, bends or en echelon step-over structures. These can host complex rupture dynamics and produce a variety of displacement patterns when ruptured, which may promote tsunami generation (Legg and Borrero, 2001; Borrero et al, 2004).

To mitigate the commonly under-represented hazard of strike-slip induced tsunamis, it is crucial to fundamentally understand the direct effect of coseismic dis-

<sup>1</sup> Department of Earth and Environmental Sciences, Ludwig-Maximilians-Universität München, Munich, Germany

<sup>2</sup> Institute of Mathematics, Freie Universität Berlin, Berlin, Germany

<sup>3</sup> Observatório Sismológico, Instituto de Geociências, Universidade de Brasília, Brasília, Brazil

<sup>4</sup> Numerical Methods in Geosciences, Department of Mathematics, Universität Hamburg, Hamburg, Germany

<sup>5</sup> Department of Earth Sciences, Utrecht University, Utrecht, The Netherlands

<sup>6</sup> Seismology and Wave Physics, Institute of Geophysics, Department of Earth Sciences, ETH Zürich, Zürich, Switzerland

<sup>7</sup> Jet Propulsion Laboratory, California Institute of Technology, Pasadena, California, USA

<sup>8</sup> Seismological Laboratory, California Institute of Technology, Pasadena, California, USA

placements on tsunami genesis. Globally, geological settings similar to that governing the Sulawesi earthquake-tsunami sequence are not unique. Large strike-slip faults crossing off-shore and running through narrow gulfs include the elongated Bodega and Tomales bays in northern California, USA, hosting major segments of the right-lateral strike-slip San Andreas fault system, and the left-lateral Anatolian fault system in Turkey, extending beneath the Marmara Sea just south of Istanbul. Indeed, historical data do record local tsunamis generated from earthquakes along these and other strike-slip fault systems, such as in the 1906 San Francisco (California), 1994 Mindoro (Philippines), and 1999 Izmit (Turkey) earthquakes (Legg et al, 2003) and, more recently, the 2016 Kaikōura, New Zealand earthquake (Ulrich et al, 2019; Power et al, 2017).

In most tsunami modelling approaches, the tsunami source is computed according to the approach of Mansinha and Smylie (1971) and subsequently parameterized by the Okada model (Okada, 1985), which translates finite fault models into seafloor displacements. Okada’s model allows computing analytically static ground displacements generated by a uniform dislocation over a finite rectangular fault assuming a homogeneous elastic half space. Heterogeneous slip can be captured by linking several dislocations in space, and time-dependence is approximated by allowing these dislocations to move in sequence (e.g., Tanioka et al, 2006). While seafloor and coastal topography are ignored, the contribution of horizontal displacements may be additionally accounted for by a filtering approach suggested by Tanioka and Satake (1996), which includes the gradient of local bathymetry. Applying a traditional Okada source to study tsunami genesis is specifically limited for near-field tsunami observations and localized events due to its underlying, simplifying assumptions.

Realistic modeling of earthquakes and tsunamis benefits from physics-based approaches. Finite fault models are affected by inherent non-uniqueness, which may spread via the ground displacement fields to the modeled tsunami genesis. Constraining the kinematics of multi-fault rupture is especially challenging, since initial assumptions on fault geometry strongly affect the slip inversion results. Mechanically viable earthquake source descriptions are provided by dynamic rupture modeling combining spontaneous frictional failure and seismic wave propagation. Dynamic rupture simulations fully coupled to the time-dependent response of an overlying water layer have been performed by Lotto et al (2017a,b, 2018). These have been instrumental in determining the influence of different earthquake parameters and material properties on coupled systems, but are restricted to 2D. Ryan et al (2015) couple a 3D dynamic earth-

quake rupture model to a tsunami model, but these are restricted to using the final, static seafloor displacement field as the tsunami source.

To capture the physics of the interaction of the Palu earthquake and tsunami we utilize a physics-based, coupled earthquake-tsunami model. The dynamic earthquake rupture model incorporates spatial variation in subsurface material properties, spontaneously developing slip on a complex, non-planar system of 3D faults, off-fault plastic deformation, and the non-linear interaction of frictional failure with seismic waves. The coseismic deformation of the crust generates time-dependent seafloor displacements, which we translate into bathymetry perturbations to source the tsunami. The tsunami model solves for non-linear wave propagation and inundation at the coast.

Using this coupled approach, we evaluate the influence of coseismic deformation during the strike-slip Sulawesi earthquake on generating the observed tsunami waves. The physics-based model reveals that the rupture of a fault crossing Palu Bay with a moderate but wide-spread component of normal fault slip produces vertical deformation, which can explain the observed tsunami wave amplitudes and wave run-up heights.

## 2 The 2018 Palu, Sulawesi earthquake and tsunami

### 2.1 Tectonic setting

The Indonesian island of Sulawesi is located at the triple junction between the Sunda plate, the Australian plate and the Philippine Sea plate (Bellier et al, 2006; Socquet et al, 2006, 2019) (Fig. 1a). Convergence of the Philippine and Australian plates toward the Sunda plate is accommodated by subduction and rotation of the Molucca Sea, Banda Sea and Timor plates, leading to complicated patterns of faulting (Fig. 1a).

In central Sulawesi, the NNW-striking Palu-Koro fault (PKF) and the WNW-striking Matano faults (MF) (Fig. 1a) comprise the Central Sulawesi Fault System. The Palu-Koro fault runs off-shore to the north of Sulawesi through the narrow Palu Bay and is the fault that hosted the earthquake that occurred on 28 September 2018. With a relatively high slip rate of 40 mm/yr inferred from recent geodetic measurements (Socquet et al, 2006; Walpersdorf et al, 1998) and clear evidence for Quaternary activity (Watkinson and Hall, 2017), the Palu-Koro fault was presumed to pose a threat to the region (Watkinson and Hall, 2017). In addition, four tsunamis associated with earthquakes on the Palu-Koro fault have struck the northwest coast of Sulawesi in the

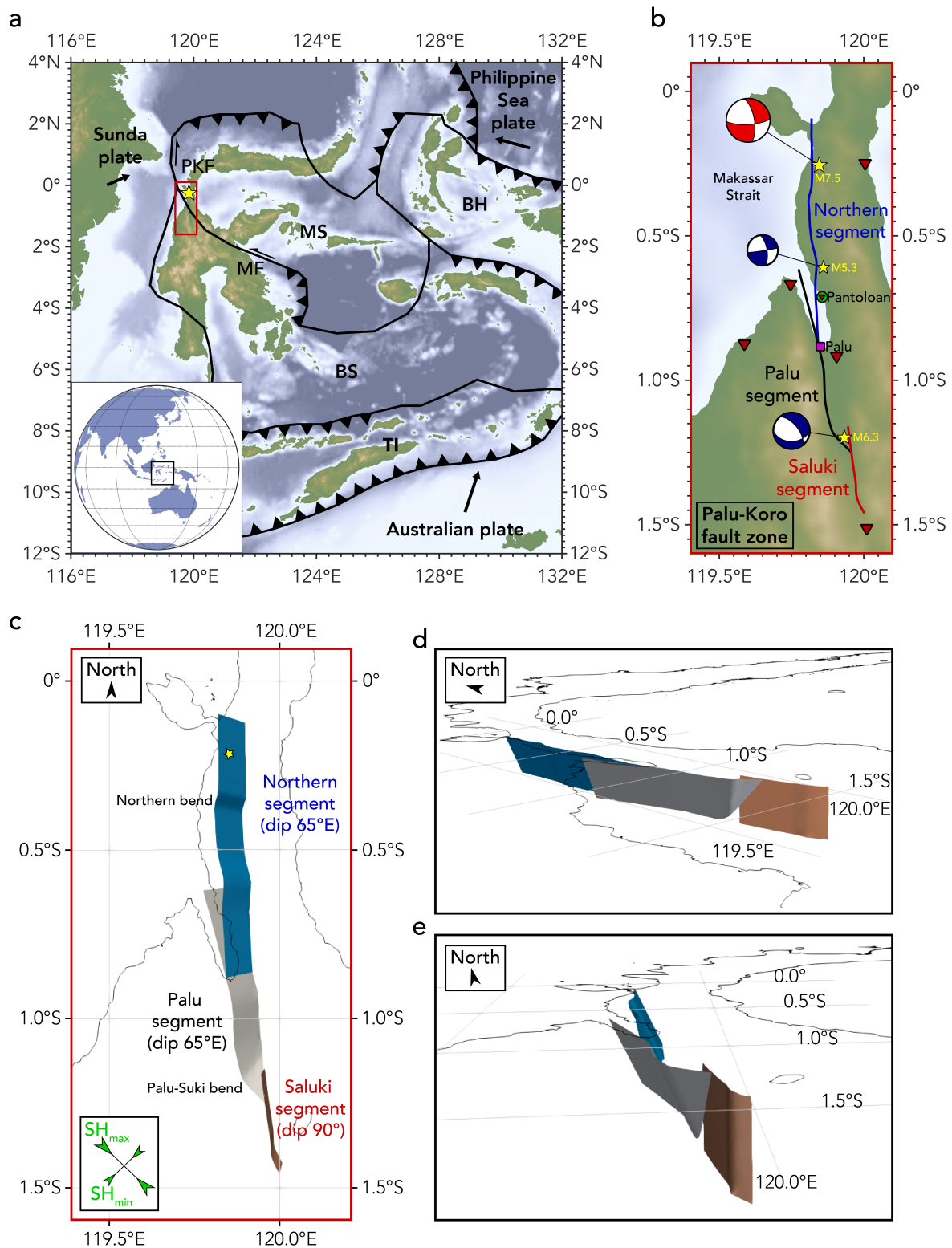


**Fig. 1** (a) Tectonic setting of the September 28, 2018  $M_w$  7.5 Sulawesi earthquake (epicenter indicated by yellow star). Black lines indicate plate boundaries based on Bird (2003); Argus et al (2011). Abbreviations: BH – Bird’s Head plate; BS – Banda Sea plate; MF – Matano fault zone; PKF – Palu-Koro fault zone; MS – Molucca Sea plate and TI – Timor plate. Arrows indicate the far-field plate velocities with respect to Eurasia (Socquet et al, 2006). The red box corresponds to the zoom-in region displayed in (b). (b) A zoom of the region of interest. The site of the harbor tide gauge of Pantoloan is indicated as well as the city of Palu. Locations of the GPS stations at which we provide synthetic ground displacement time series (see Appendix Sec.8.2) are indicated by the red triangles. Focal mechanisms and epicenters of the September 28, 2018 Palu earthquake (USGS (2018a), top), October 1, 2018 Palu aftershock (middle), and January 23, 2005 Sulawesi earthquake (bottom) are shown. These later two events provide constraints on the dip angles of individual segments of the fault network. Individual fault segments of the Palu-Koro fault used in the dynamic rupture model are coloured. (c), (d) and (e) 3D model of the fault network viewed from top, SW and S.

past century (1927, 1938, 1968 and 1996) (Pelinovsky et al, 1997; Prasetya et al, 2001).

The complex regional tectonics subject northwestern Sulawesi to transtensional strain (Socquet et al, 2006). Transtension promotes some component of dip-slip faulting on the predominantly strike-slipping Palu-Koro fault (Bellier et al, 2006; Watkinson and Hall, 2017) and leads to more complicated surface deformation than is expected from slip along a fault hosting purely strike-slip motion.

## 2.2 The 2018 Palu, Sulawesi earthquake

The  $M_w$  7.5 Sulawesi earthquake that occurred on September 28, 2018 ruptured a 180 km long section of Palu-Koro fault (Socquet et al, 2019). It nucleated 70 km north of the city of Palu at shallow depth, with inferred hypocentral depths varying between 10 km and 22 km (Valkaniotis et al, 2018). The rupture propagated predominantly southward, passing under Palu Bay and the city of Palu. It arrested after a total rupture time of 30–40 seconds (Socquet et al, 2019; Okuwaki et al, 2018; Bao et al, 2019).

The earthquake appears to have propagated at a supershear rupture speed, i.e., faster than the shear waves produced by the earthquake are able to travel through the surrounding rock (e.g., Socquet et al, 2019; Bao et al, 2019; Mai, 2019). Socquet et al (2019) note that the characteristics of the relatively straight, clear rupture trace to the south of the Bay, with few aftershocks, match those for which supershear rupture speeds have been inferred in other earthquakes. Using back-projection analysis, which maps the location and timing of earthquake energy from the waves recorded on distant seismic arrays, Bao et al (2019) do not resolve any portion of the rupture as traveling at sub-Rayleigh speeds. The authors conclude that this fast rupture velocity began at, or soon after, earthquake nucleation and was sustained for the length of the rupture. Surprisingly, Bao et al (2019) infer supershear rupture speeds at the lower end considered theoretically stable, possibly due to the influence of widespread, pre-existing damage around the fault. While the actual speed, point of onset, and underlying mechanics of this event’s supershear rupture propagation remain to be studied further, it will initiate re-assessment of hazard associated with strike-slip faults worldwide with respect to the potential intensification of supershear shaking.

## 2.3 The induced tsunami

The Palu earthquake triggered a local but powerful tsunami that devastated the coastal area of the Palu Bay quickly after the earthquake. Inundation depths of over 6 m and run-up heights of over 9 m were recorded at specific locations (e.g. Yalciner et al, 2018). At the only tide gauge with available data, located at Pantoloan harbor, a trough-to-peak wave amplitude of almost 4 m was recorded just five minutes after the rupture (Muhari et al, 2018). In Ngapa (Wani), on the northeastern shore of Palu Bay, CCTV coverage show the arrival of the tsunami wave after only 3 minutes.

Coseismic subsidence and uplift, as well as submarine and coastal landsliding, have been suggested as causes of the tsunami in Palu Bay (Heidarzadeh et al, 2018). Both displacements and landsliding are documented on land (Valkaniotis et al, 2018; Løvholt et al, 2018; Sassa and Takagawa, 2019), and also at coastal slopes (Yalciner et al, 2018).

Tsunami models of the Sulawesi event performed using Okada’s solution in combination with the USGS finite fault model (USGS, 2018b) do not generate tsunami amplitudes large enough to agree with observations (Heidarzadeh et al, 2018; Sepulveda et al, 2018; Liu et al, 2018; van Dongeren et al, 2018). Liu et al (2018) and Sepulveda et al (2018) perform Okada-based tsunami modeling with earthquake sources generated by inverting satellite data, but also produce wave amplitudes that are too small. Reasonable tsunami waves are produced by combining tectonic and hypothetical landslide sources (van Dongeren et al, 2018; Liu et al, 2018). However, the predominantly short wavelengths associated with the observed small scale, localized landsliding (Yalciner et al, 2018) appears to be incompatible with the observed long period tsunami waves (Løvholt et al, 2018).

## 3 Physical and Computational Models

### 3.1 Earthquake-tsunami modeling within the ASCETE framework

The ASCETE framework (Advanced Simulation of Coupled Earthquake and Tsunami Events; see Gabriel et al, 2018) establishes methods for coupling physics-based models of geodynamic subduction zone processes, seismic cycling, dynamic earthquake rupture, and tsunami propagation and inundation. Here, we apply part of the framework to model the coupling between a single dynamic earthquake rupture and the resulting occurrence of a tsunami.

Since the earthquake and tsunami communities use different vocabulary, we specify the terminology used



throughout this manuscript. We call the complete physical setup, including, e.g., the bathymetry dataset, fault structure and the governing equations for an earthquake or tsunami, a ‘physical model’. Furthermore, a computer program discretizing the equations and implementing the numerical workflow is termed a ‘computational model’. The result of a computation for a specific event achieved with a computational model and according to a specific physical model will be called a ‘scenario’. We use ‘model’ where the use of the term as either physical or computational model is unambiguous.

The computational model used to produce the earthquake scenario is SeisSol (Dumbser and Käser, 2006; Pelties et al, 2014; Uphoff et al, 2017), which solves the elastodynamic wave equation. SeisSol solves for spontaneous dynamic rupture and seismic wave propagation to determine the temporal and spatial evolution of slip on predefined frictional interfaces, and the stress and velocity fields throughout the modeling domain. With this approach, the earthquake source is not predetermined, but evolves spontaneously as a consequence of the model’s initial conditions and of the time-dependent, non-linear processes occurring during the earthquake. Initial conditions include the geometry and frictional strength of the fault(s), the tectonic stress state, and the regional lithological structure. Fault slip evolves as frictional shear failure according to an assigned friction law that controls how the fault yields and slides. Model outputs include spatial and temporal evolution of the earthquake rupture front(s), off-fault plastic strain, surface displacements, and the ground shaking caused by the radiated seismic waves.

SeisSol uses the Arbitrary high-order accurate Derivative Discontinuous Galerkin method (ADER-DG). It employs fully non-uniform, unstructured tetrahedral meshes to combine geometrically complex 3D geological structures, nonlinear rheologies, and high-order accurate propagation of seismic waves. Fast time to solution is achieved thanks to end-to-end computational optimization (Breuer et al, 2014; Heinecke et al, 2014; Rettenberger et al, 2016) and an efficient local time-stepping algorithm (Uphoff et al, 2017). To this end, dynamic rupture simulations can reach high spatial and temporal resolution of increasingly complex geometrical and physical modelling components (e.g. Bauer et al, 2017; Wollherr et al, 2018a). SeisSol is verified with a wide range of community benchmarks, including strike-slip, dipping and branching fault geometries, laboratory derived friction laws, as well as heterogeneous on-fault initial stresses and material properties (de la Puente et al, 2009; Pelties et al, 2012, 2013, 2014; Wollherr et al, 2018b) in line with the SCEC/USGS Dynamic Rupture Code Verification exercises (Harris et al, 2011, 2018).

SeisSol is freely available (SeisSol website, 2019; SeisSol github, 2019).

The computational model to generate the tsunami scenario is StormFlash2D, which solves the nonlinear shallow water equations using an explicit Runge-Kutta discontinuous Galerkin discretization combined with a sophisticated wetting and drying treatment for the inundation at the coast (Vater and Behrens, 2014; Vater et al, 2015, 2017). A tsunami is triggered by a (possibly time-dependent) perturbation of the discrete bathymetry. StormFlash2D allows for stable and accurate simulation of large-scale wave propagation in deep sea, as well as small-scale wave shoaling and inundation at the shore, thanks to a multi-resolution adaptive mesh refinement approach based on a triangular refinement strategy (Behrens et al, 2005; Behrens and Bader, 2009). Bottom friction is parameterized through Manning friction by a split-implicit discretization (Liang and Marche, 2009). The model’s applicability for tsunami events has been validated by a number of test cases (Vater et al, 2018), which are standard for the evaluation of operational tsunami codes (Synolakis et al, 2007).

Coupling between the earthquake and tsunami models is realized through the time-dependent coseismic 3D seafloor displacement field computed in the dynamic earthquake rupture scenario, which is translated into 2D bathymetry perturbations of the tsunami model.

### 3.2 Earthquake model

The 3D dynamic rupture model of the Sulawesi earthquake requires initial assumptions related to the structure of the Earth, the structure of the fault system, the stress state, and the frictional strength of the faults. These input parameters are constrained by a variety of independent near-source and far-field data sets. Most importantly, we aim to ensure mechanical viability by a systematic approach integrating the observed regional stress state and frictional parameters and including state-of-the-art earthquake physics and fracture mechanics concepts in the model (Ulrich et al, 2019).

#### 3.2.1 Earth structure

The earthquake model incorporates topography and bathymetry data and state-of-the-art information about the subsurface structure in the Palu region. Local topography and bathymetry are honored at a resolution of about 900 m (GEBSCO, 2015; Weatherall et al, 2015). At depth, 3D heterogeneous media are included by combining two subsurface velocity data sets. A local model by Awaliah et al (2018), which is built from ambient noise tomography, covers the model domain down to 40 km

depth. The Global Earth Model (Fichtner et al, 2018) is used to cover the model domain down to 150 km.

### 3.2.2 Fault structure

For this model, we construct a network of non-planar, intersecting crustal faults that ruptured in this earthquake. This includes three major fault segments: the Northern segment, a previously unmapped fault on which the earthquake nucleated, and the Palu and the Saluki segments of the Palu-Koro fault (cf. Fig. 1b-e). We map the fault traces from the horizontal ground displacement field inferred from correlation of Sentinel-2 optical images (De Michele, 2018) and from synthetic aperture radar (SAR) data (Bao et al, 2019), which is discussed more below. Differential north-south offsets clearly delineate the on-land traces of the Palu and Saluki fault segments. The trace of the Northern segment is less well-constrained in both data sets. Nevertheless, we produce a robust map by honoring the clearest features in both datasets and smoothing regions of large variance using QGIS v2.14 (Quantum, 2013).

Beneath the Bay, we adopt a relatively simple fault geometry motivated by the on land fault strikes, the homogeneous pattern of horizontal ground deformation east of the Bay (De Michele, 2018), which suggests slip on a straight, continuous fault under the Bay, and the absence of direct information available to constrain the rupture’s path. We extend the Northern segment southward as a straight line from the point where it enters the Bay to the point where the Palu segment enters the Bay. We extend the Palu segment northward, adopting the same strike that it displays on land to the south of the Bay. This trace deviates a few km from the mapping reported in Bellier et al (2006, their Fig. 2), both on and off land. South of the Bay, the modeled segment mostly aligns with the fault as mapped by Watkinson and Hall (2017, their Fig. 5).

We constrain the 3D structure of these faults using focal mechanisms and geodetic data. We assume that the Northern and Palu segments both dip  $65^\circ$  East, as suggested by the mainshock focal mechanisms ( $67^\circ$ , USGS (2018a) and  $69^\circ$ , IGP (2018), Fig. 1b) and the focal mechanism of the 2018, October 1st  $M_w$  5.3 aftershock ( $67^\circ$ , BMKG solution, Fig. 1b). This also is consistent with pronounced asymmetric patterns of ground deformation suggesting slip on dipping faults around the city of Palu and the Northern fault segment in both the optical De Michele (2018) and SAR data. In addition, the eastward dip of the Palu segment on land is consistent with the analysis of Bellier et al (2006). The southern end of the Palu segment bends towards the Saluki segment and features a dip of  $60^\circ$  to the

northeast, as constrained by the source mechanism of the 2005  $M_w$  6.3 event (see Fig. 1b). In contrast, we assume that the Saluki segment is vertical. The assigned dip of  $90^\circ$  acknowledges the inferred ground deformation of comparable amplitude and extent on both sides of this fault segment (De Michele, 2018). All faults reach a depth of 20 km.

### 3.2.3 Stress state

The fault system is subject to a laterally homogeneous regional stress field, systematic constraints based on seismo-tectonic observations, fault fluid pressurization and the Mohr-Coulomb theory of frictional failure following Ulrich et al (2019). This is motivated by the fact that tractions on and strength of natural faults are difficult to quantify. With this approach, only four parameters must be specified to fully describe the state of stress and strength governing the fault system, as further detailed in the appendix (Sec. 8.3). This systematic approach facilitates rapid modeling of an earthquake.

Using static considerations and few trial dynamic simulations, we identify an optimal stress configuration for this scenario that simultaneously (i) maximizes the ratio of shear over normal stress all across the fault system; (ii) determines shear traction orientations that predict surface deformation compatible with the measured ground deformation and focal mechanisms; and (iii) allows dynamic rupture across the fault system’s geometric complexities.

The resulting physical model is characterized by a stress regime acknowledging transtension, high fluid pressure, and relatively well oriented, apparently weak faults. The effective confining stress increases with depth by a gradient of 5.5 MPa/km. From 11–15 km depth, we taper the deviatoric stresses to zero, to represent the transition from a brittle to a ductile deformation regime. The depth range is consistent with the 12 km interseismic locking depth estimated by Vigny et al (2002).

### 3.2.4 Earthquake nucleation and fault friction

Failure is initiated within a highly overstressed circular patch with a radius of 1.5 km situated at a depth of 10 km. This depth is at the shallow end of the range of inferred hypocentral depths (Valkaniotis et al, 2018) and shallower than the modeled brittle-ductile transition mimicking the lower end of the seismogenic zone.

Slip evolves on the fault according to a rapid velocity-weakening friction formulation, which is motivated by laboratory experiments that show strong dynamic weakening at coseismic slip rates (e.g., Di Toro et al, 2011).

455 This formulation reproduces realistic rupture charac-  
 456 teristics, such as reactivation and pulse-like behavior,  
 457 without imposing small-scale heterogeneities (e.g., Dun-  
 458 ham et al, 2011; Gabriel et al, 2012). We here use a form  
 459 of fast-velocity weakening friction proposed in the com-  
 460 munity benchmark problem TPV104 of the Southern  
 461 California Earthquake Center (Harris et al, 2018) and  
 462 as parameterized by Ulrich et al (2019). Friction drops  
 463 rapidly from a steady-state, low-velocity friction coeffi-  
 464 cient, here 0.6, to a fully weakened friction coefficient,  
 465 here 0.1 (see Sec. 8.4).

### 466 3.2.5 Model resolution

467 A high resolution computational model is crucial in  
 468 order to accurately resolve the full dynamic complexity  
 469 of our earthquake scenario. The required high numerical  
 470 accuracy is achieved by combining a numerical scheme  
 471 that is accurate to high-orders and a mesh that is locally  
 472 refined around the fault network.

473 The earthquake model domain is discretized into an  
 474 unstructured computational mesh of 8 million tetrahe-  
 475 dral elements. The shortest element edge lengths are  
 476 200 m close to faults. The static mesh resolution is coars-  
 477 ened away from the fault system. Simulating 50 s of  
 478 this event using 4th order accuracy in space and time  
 479 requires about 2.5 hours on 560 Haswell cores of phase  
 480 2 of the SuperMUC supercomputer of the Leibniz Su-  
 481 percomputing Centre in Garching, Germany. We point  
 482 out that running hundreds of such simulations is well  
 483 within the scope of resources available to typical users  
 484 of supercomputing centres.

### 485 3.3 Tsunami model

486 The bathymetry and topography for the tsunami model  
 487 is composed with the high-resolution data set BAT-  
 488 NAS (v1.0), provided by the Indonesian Geospatial Data  
 489 Agency (DEMNAS, 2018). This data set has a horizon-  
 490 tal resolution of 6 arc seconds (or approximately 190 m),  
 491 and it allows for sufficiently accurate representation of  
 492 bathymetric features, but is certainly relatively inaccur-  
 493 ate with respect to inundation treatment.

494 The coupling between the earthquake and tsunami  
 495 models is enforced by adding a perturbation derived  
 496 from the 3D coseismic seafloor displacement from the dy-  
 497 namic rupture scenario to the initial 2D bathymetry and  
 498 topography of the tsunami model. These time-dependent  
 499 displacement fields are given by the three-dimensional  
 500 vector  $(\Delta x, \Delta y, \Delta z)$ . Additionally to the vertical dis-  
 501 placement  $\Delta z$ , we incorporate the horizontal compo-  
 502 nents  $\Delta x$  and  $\Delta y$  into the tsunami source by applying  
 503 the method proposed by Tanioka and Satake (1996).

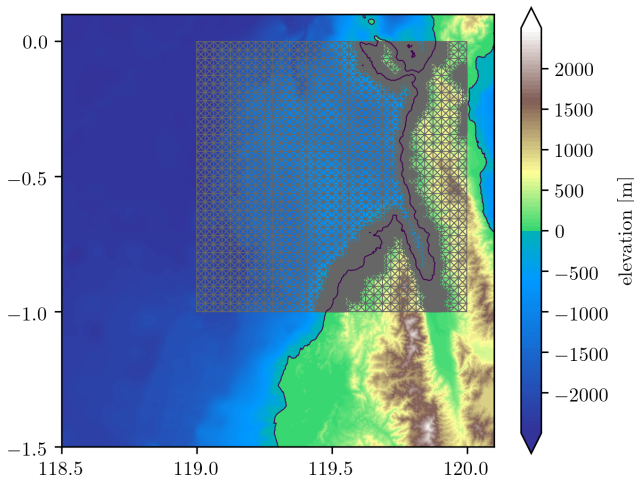


**Fig. 2** Setup of the tsunami model including high-resolution bathymetry and topography data overlain by the initial adaptive triangular mesh refined near the coast.

504 This is motivated by the potential influence of Palu  
 505 Bay’s steep seafloor slopes (more than 50%). The ground  
 506 displacement of the earthquake model is translated into  
 507 the tsunami generating bathymetry perturbation by

$$508 \Delta b = \Delta z - \Delta x \frac{\partial b}{\partial x} - \Delta y \frac{\partial b}{\partial y}, \quad (1)$$

509 where  $b = b(x, y)$  is the bathymetry (increasing in the  
 510 upward direction).  $\Delta b$  is time-dependent, since  $\Delta x$ ,  $\Delta y$   
 511 and  $\Delta z$  are time-dependent (cf. Fig. S2). The tsunami is  
 512 sourced by adding  $\Delta b$  to the initial bathymetry and to-  
 513 pography of the tsunami model. It should be noted that  
 514 a comparative scenario using only  $\Delta z$  as bathymetry  
 515 perturbation (see appendix, Sec. 8.5) did not result in  
 516 large deviations with regards to the preferred model.

517 The domain of the computational tsunami model  
 518 (latitudes ranging from  $-1^\circ$  to  $0^\circ$ , longitudes ranging  
 519 from  $119^\circ$  to  $120^\circ$ , see Fig. 2) encompasses Palu Bay  
 520 and its near surroundings in the Makassar Strait, since  
 521 we here focus on the wave behavior within the Bay of  
 522 Palu. The tsunami model is initialized as an ocean at  
 523 rest, for which (at  $t = 0$ ) the initial fluid depth is set in  
 524 such manner that the sea surface height (ssh, deviation  
 525 from mean sea level) is equal to zero everywhere in  
 526 the model domain. Additionally, the fluid velocity is  
 527 set to zero. This defined initial steady state is then  
 528 altered by the time-dependent bathymetry perturbation  
 529 throughout the simulation, which triggers the tsunami.  
 530 The simulation is run for 40 min (simulation time),  
 531 which needs 13 487 time steps.

532 The triangle-based computational grid is initially re-  
 533 fined near the coast, where the highest resolution within  
 534 Palu Bay is about 3 arc seconds (or 80 m). This results

in an initial mesh of 153 346 cells, which expands to more than 300 000 cells during the dynamically adaptive computation. The refinement strategy is based on the gradient in sea surface height (ssh).

The parametrization of bottom friction includes the Manning’s roughness coefficient  $n$ . We assume  $n = 0.03$ , which is a typical value for tsunami simulations (Harig et al, 2008).

## 4 Results

In the following, we present a well-constrained, physics-based, coupled earthquake and tsunami model scenario explaining local and far-field seismic and tsunami observations.

### 4.1 The dynamic earthquake rupture scenario: sustained supershear rupture and normal slip component within Palu Bay

Based on a systematic derivation of initial conditions (Sec. 3.2), we find that early and persistent supershear rupture is required to reproduce seismological data, geodetic data, as well as field observations in the near- and far-field. The model produces moderate vertical displacements beneath Palu Bay due to oblique slip on a dipping fault, even though it does not feature significant submarine geometric complexities.

#### 4.1.1 Earthquake rupture

The dynamic earthquake scenario is characterized by an unilateral southward rupture (Fig. 3). The rupture nucleates at the northern tip of the Northern segment, then transfers to the Palu segment at the southern end of Palu Bay, on which it propagates also unilaterally southward. Additionally, a shallow portion of the Palu-Koro fault beneath the Bay ruptures from North to South (see inset of Fig. 4a). This segment is dynamically unclamped (due to reduced normal stress) while the rupture of the Northern segment passes. The rupture passes from the Palu segment onto the Saluki segment through a restraining bend at a latitude of  $-1.2^\circ$ . In total, 195 km of faults are ruptured leading to a  $M_w$  7.6 earthquake scenario.

#### 4.1.2 Fault slip

The modeled slip distributions and orientations (Fig. 4) are modulated by the geometric complexities of the fault system. On the northern part of the Northern segment, slip is lower than elsewhere along the fault due to a

restraining fault bend near  $-0.35^\circ$  latitude (Fig. 4a). South of this small bend, the slip magnitude increases and remains mostly homogeneous, ranging between 6 and 8 m. Peak slip occurs on the Palu segment.

Over most of the fault network, the faulting mechanism is predominantly strike-slip, but does include a small to moderate normal slip component (Fig. 4b). This dip-slip component varies as a function of fault orientation with respect to the regional stress field. It increases at the junction between the Northern and Palu segment just south of Palu Bay, and at the big bend between the Palu and Saluki fault segments, where dip-slip reaches a maximum of approx. 4 m. Pure strike-slip faulting is modeled on the southern part of the vertical Saluki segment (Fig. 4b). The dip-slip component along the rupture shown in Fig. 4b produces subsidence above the hanging wall (east of the fault traces) and uplift above the foot wall (west of the fault traces). The resulting seafloor displacements are further discussed in Sec. 4.2.

#### 4.1.3 Earthquake rupture speed

The earthquake scenario features an early and persistent supershear rupture velocity (Fig. 4d). This means that the rupture speed exceeds the seismic shear wave velocity ( $V_s$ ) of 2.5 to 3.1 km/s in the vicinity of the fault network from the onset of the event. This agrees with the inferences for supershear rupture by Bao et al (2019) from back-projection analyses and by Socquet et al (2019) from satellite data analyses. However, we here infer supershear propagation faster than Eshelby speed ( $\sqrt{2}V_s$ ), and thus faster than Bao et al (2019), well within the stable supershear rupture regime (Burridge, 1973).

#### 4.1.4 Teleseismic waves, focal mechanism, and moment release rate

The dynamic rupture scenario satisfactorily reproduces the teleseismic surface waves (Fig. 5a) and body waves (Fig. 5b). Synthetics are generated at 5 teleseismic stations around the event (Fig. 5c). Following Ulrich et al (2019), we translate the dynamic fault slip time histories of the dynamic rupture scenario into a subset of 40 double couple point sources (20 along strike times 2 along depth). From these sources, broadband seismograms are calculated from a Green’s function database using Instaseis (Krischer et al, 2017) and the PREM model for a maximum period of 2 s and including anisotropic effects. Our synthetics agree well with the observed teleseismic signals in terms of both the dominant, long-period surface waves and the body wave signatures.

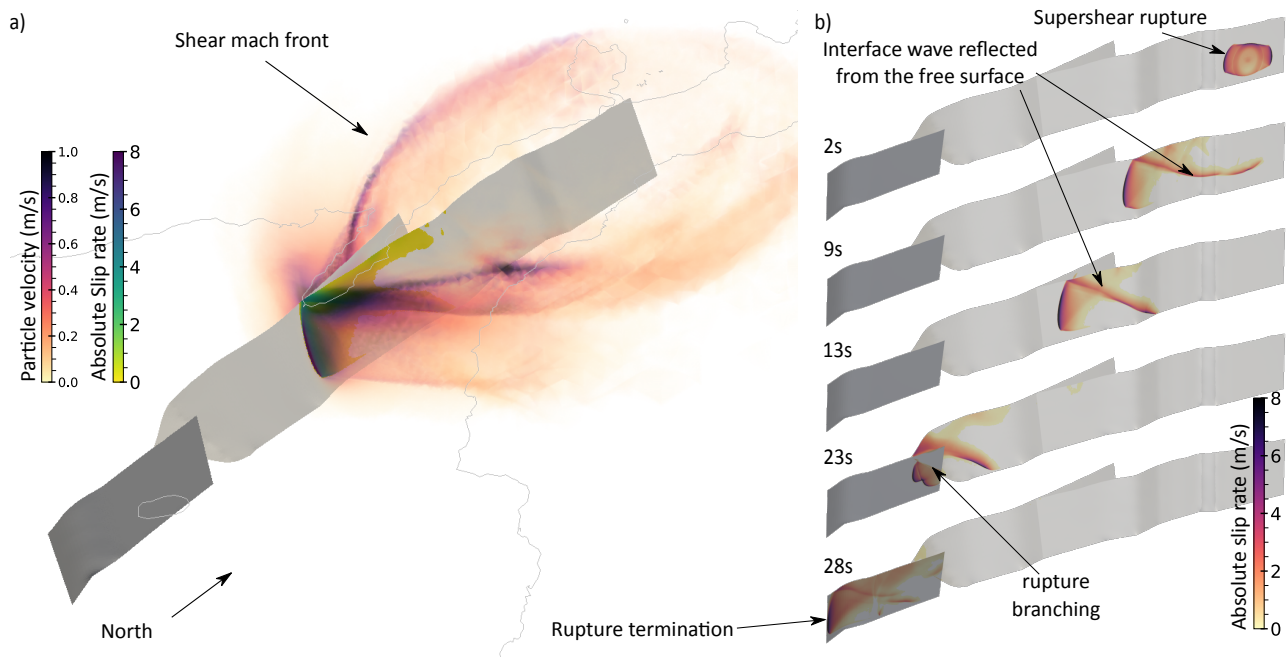


**Fig. 3** (a) Snapshot of the wavefield (absolute particle velocity in m/s) and the slip rate (in m/s) across the fault network at a rupture time of 15 s. (b) Overview of the simulated rupture propagation. Snapshots of the absolute slip rate are shown at a rupture time of 2, 9, 13, 23 and 28 s. Labels indicate noteworthy features of the rupture.

627 The focal mechanism of the modeled source is com-  
 628 patible with the one inferred by USGS (compare Fig. 1b  
 629 and Fig. 5c). The nodal plane characterizing this model  
 630 features strike/dip/rake angles of  $354^\circ/69^\circ/-14^\circ$ , which  
 631 is very close to the  $350^\circ/67^\circ/-17^\circ$  focal plane inferred  
 632 by USGS.

633 The dynamically released moment rate is in agree-  
 634 ment with source time functions inferred from tele-  
 635 seismic data (Fig 5d). Our scenario yields a relatively  
 636 smooth, roughly box-car shaped moment release rate  
 637 spanning the full rupture duration. This is consistent  
 638 with Okuwaki et al (2018)'s inference and consistent  
 639 with the smooth inferred fault slip reported by Socquet  
 640 et al (2019). Interestingly, we can identify a pronounced  
 641 effect of the rupture slowing down at the geometrical  
 642 complexity posed by the Northern segment restraining  
 643 bend at  $-0.35^\circ$  latitude. This resembles the moment rate  
 644 solutions by USGS and SCARDEC at  $\approx 5$  s rupture  
 645 time. The transfer of the rupture from the Palu segment  
 646 to the Saluki segment at 23 s produces a transient de-  
 647 crease in the moment release rate in our model. This  
 648 feature is discernible in observations as well.

#### 649 4.1.5 Earthquake surface displacements

650 We use observations from optical and radar satellites,  
 651 both sensitive to the horizontal coseismic surface dis-  
 652 placements, to validate the outcomes of the earthquake  
 653 scenario.

654 The patterns and magnitudes of the final horizon-  
 655 tal surface displacements in two dimensions (black ar-  
 656 rows in Fig. 6a) are inferred from subpixel correlation  
 657 of coseismic optical images acquired by the Coperni-  
 658 cus Sentinel-2 satellites by the European Space Agency  
 659 (ESA) (De Michele, 2018). We use both, east-west and  
 660 north-south components from optical image correlation.

661 We also infer coseismic surface displacements by in-  
 662 coherent cross correlation of synthetic aperture radar  
 663 (SAR) images acquired by the Japan Aerospace Ex-  
 664 ploration Agency (JAXA) Advanced Land Observation  
 665 Satellite-2 (ALOS-2). SAR can measure surface displace-  
 666 ments horizontally in the along-track direction and in the  
 667 slant direction between the satellite and the ground that  
 668 is a combination of vertical and horizontal displacement.  
 669 Here, we use the along-track horizontal displacements  
 670 (Fig. 6c) that are nearly parallel to the strike of the fault.  
 671 Further details about our data processing approach and  
 672 the dataset used can be found in appendix Sec. 8.6.

673 The use of two independent but partially coinciding  
 674 datasets provides additional insight on data quality. We  
 675 compare the SAR data and the optical data by project-  
 676 ing the optical data into the along-track direction of the  
 677 SAR data. This allows for identification of the robust fea-  
 678 tures in the imaged surface displacements. Along most  
 679 of the rupture, fault displacements are sharp and linear,  
 680 highlighting smooth and straight fault orientations with  
 681 some bends. Both datasets appear to be consistent to  
 682 first order ( $\pm 1m$ ) in a 30 km wide area centered on the



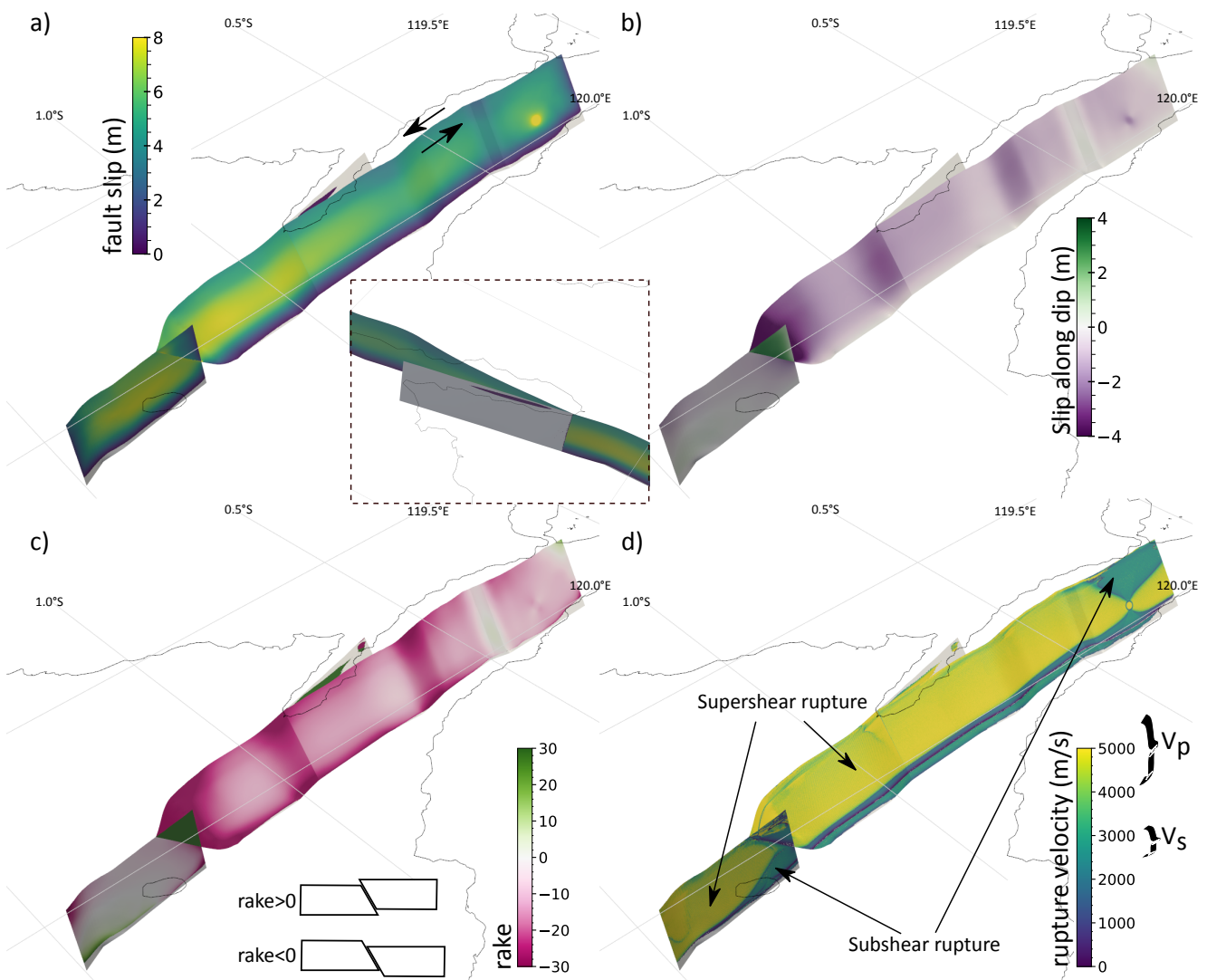


**Fig. 4** Kinematic and dynamic source properties of the dynamic rupture scenario. (a) Final slip magnitude. The inset shows the slip magnitude on the main Palu-Koro-fault within the Bay. (b) Dip-slip component. (c) Final rake angle. (b) and (c) both illustrate a moderate normal slip component. (d) Maximum rupture velocity indicating pervasive supershear rupture.

683 fault and south of  $-0.6^\circ$  latitude, as identified in Fig. 6a. North of the Bay, the optical displacements are large  
 684 in magnitude relative to the SAR measurements. Such large displacements continue north of the inferred rup-  
 685 ture trace, suggesting a bias in the optical data in this region. These large apparent displacements may be due  
 686 to partial cloud cover in the optical images or to image misalignment. The EW component seems unaffected by  
 687 this problem. Significant differences between inferences from SAR and optical data are furthermore observed  
 688 in the area near the Palu-Saluki bend. Thus, deviations between model synthetics and observational data in the  
 689 the affected areas North of the Bay will be analyzed with caution.

697 Overall, the earthquake dynamic rupture scenario matches observed ground displacements well. East of  
 698

699 the Palu segment, a good agreement between synthetic displacements and observations is achieved. Horizontal  
 700 surface displacement vectors predicted by the model are well aligned with and of comparable amplitude to optical  
 701 observations (Fig. 6a). West of the Palu segment, the modeled amplitudes are in good agreement with the SAR  
 702 and optical data, however the synthetic orientations point to the southwest, whereas the optical data are  
 703 oriented to the southeast. While surface displacement orientations around the Saluki segment are reproduced well,  
 704 amplitudes may be overestimated by about 1 m on the eastern side of the fault (Fig. 6d). North of the Bay,  
 705 the modeled amplitudes exceed SAR measurements by about 2 m. Nevertheless, the subtle eastward rotation  
 706 of the horizontal displacement vectors near the Northern  
 707  
 708  
 709  
 710  
 711  
 712  
 713

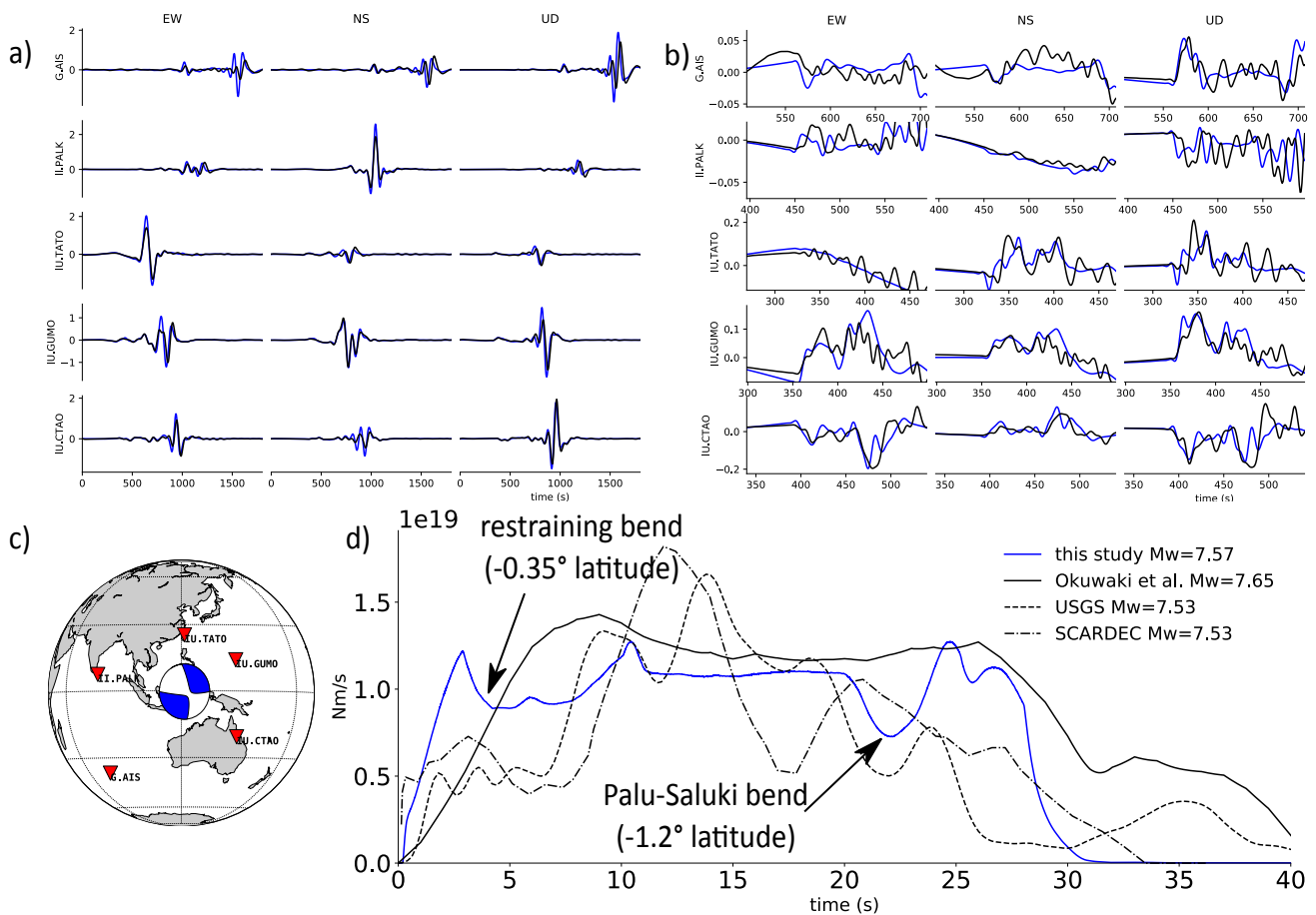


**Fig. 5** (a) and (b): Comparison of modeled (blue) and observed (black) teleseismic displacement waveforms. A 10-450 s band-pass filter is applied to all traces. (a) Full seismograms dominated by surface waves. (b) Zoom in to body wave arrivals. Synthetics are generated using Instaseis (Krischer et al, 2017) and the PREM model including anisotropic effects and a maximum period of 2 s. (c) Moment-tensor representation of the dynamic rupture scenario and locations at which synthetic data are compared with observed records. (d) Synthetic moment rate release function compared with those observationally inferred from teleseismic data by Okuwaki et al (2018), USGS and by the SCARDEC method (optimal solution, Vallée et al, 2011)

714 segment bend (at  $-0.35^\circ$  latitude) is captured well by  
715 the scenario.

#### 716 4.2 Tsunami propagation and inundation: an 717 earthquake-induced tsunami

718 The surface displacements induced by the earthquake  
719 result in a bathymetry perturbation  $\Delta b$  (as defined in  
720 Eq. (1)), which is visualized after 50 s simulation time  
721 (equal to earthquake rupture time) in Fig. 7a. In general,  
722 the bathymetry perturbation shows subsidence east of the  
723 faults and uplift west of the faults. The additional  
724 bathymetry effect present through the approach of Tan-  
725 ioka and Satake (1996) locally modulates the smooth  
726 displacement fields from the earthquake rupture scenario  
727 (cf. Fig. S5). Four cross-sections of the final perturbation  
728 in W-E direction are shown in Fig. 7b which capture

729 the area of Palu Bay and clearly show the step induced  
730 by the normal slip component. The variation along the  
731 fault is displayed in Fig. 7c. The step varies between  
732 0.8 m and 2.8 m, with an average of 1.5 m. Note, that  
733 this step is essentially defined as fault throw in struc-  
734 tural geology. However, here we explicitly incorporate  
735 effects of bathymetry and thus refer to the resulting  
736 seafloor perturbation.

737 The tsunami generated in this scenario is mostly  
738 localized in Palu Bay, which is illustrated in snapshots  
739 of the dynamically adaptive tsunami simulation after  
740 20 s and 600 s simulation time in Fig. 8. This is expected  
741 as the modeled fault system is offshore only within  
742 the Bay. At 20 s, the seafloor displacement due to the  
743 earthquake is clearly visible in the sea surface height  
744 (ssh) within Palu Bay. Additionally, the effect of a small  
745 uplift is visible along the coast north of the Bay. The  
746 local behavior within Palu Bay is displayed in Fig. 9



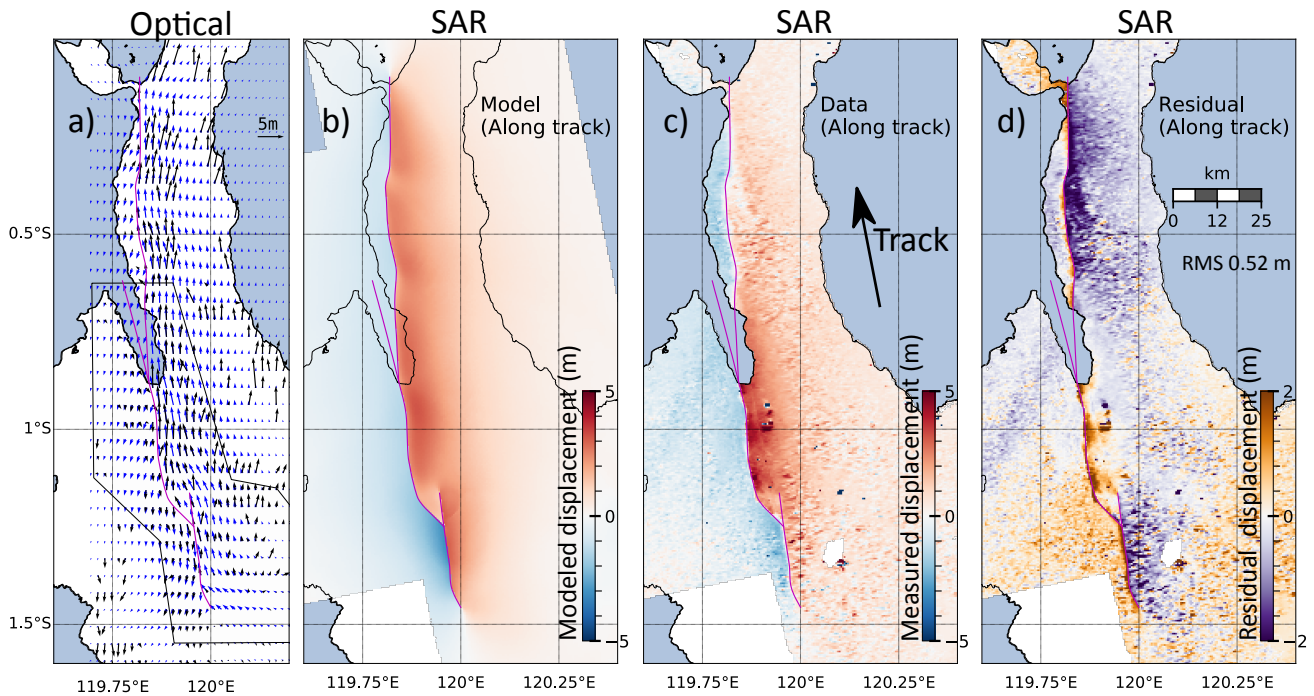


**Fig. 6** (a) Comparison of the modeled and inferred horizontal surface displacements from subpixel correlation of Sentinel-2 optical images by De Michele (2018). Some parts of large inferred displacements, e.g., north of  $-0.5^\circ$  latitude, are probably artifacts, because they are not visible in SAR data. The area inside the black polygon highlights where an at least first order agreement between SAR and optical data is achieved. Our (b) modeled and (c) measured ground displacements in the SAR satellite along-track direction (see text). (d) residual = (c) - (b).

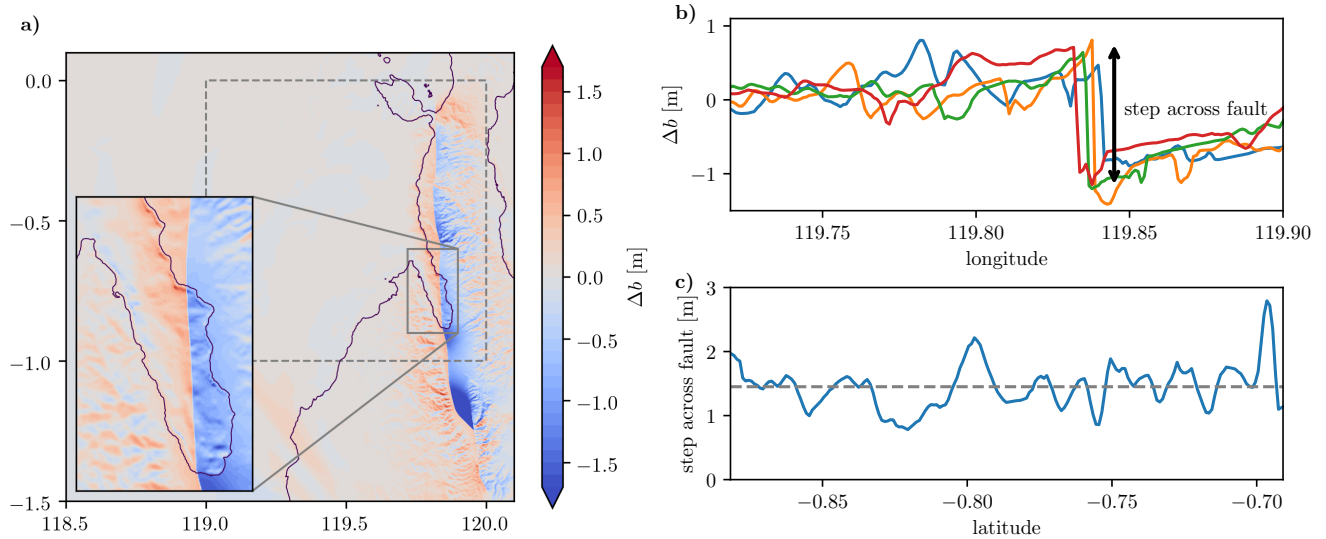


**Fig. 7** (a) Snapshot of the computed bathymetry perturbation  $\Delta b$  used as input for the tsunami model. The snapshot corresponds to a 50 s simulation time at the end of the earthquake scenario. (b) W-E cross-sections of the bathymetry perturbation at  $-0.85^\circ$  (blue),  $-0.8^\circ$  (orange),  $-0.75^\circ$  (green),  $-0.7^\circ$  (red) latitude showing the induced step in bathymetry perturbation across the fault. (c) step in bathymetry perturbation (as indicated in panel (b)) as function of latitude. Grey dashed line shows the average.

at 20 s, 180 s and 300 s. The local extrema along the coast reveal the complex wave reflections and refractions within the Bay caused by complex, shallow bathymetry as well as funnel effects.

We compare the tsunami modeling results with observational data based mainly on the comprehensive overview of run-up data, inundation data, and arrival times of tsunami waves around the shores of the Palu Bay compiled by Yalciner et al (2018). In view of the available, relatively low resolution topography data, we conduct a macro-scale comparison between the scenario and the inundation data, rather than point-wise comparison. Additionally, we compare the synthetic time series of the Pantoloan harbor tide gauge at (119.856155°E, 0.71114°S) to the observational gauge data, which has a 1-minute sampling rate. The observational time series was detided by a low-pass filter eliminating wave periods above 2 hours.

The Pantoloan tide gauge is the only tide gauge with available data in Palu Bay. The instrument is installed on a pier in Pantoloan harbor and thus records the change of water height with respect to a pier moving synchronous with the land. It recorded the tsunami with a leading trough arriving five minutes after the earthquake onset time (Fig. 10). The first and highest wave arrived approximately eight minutes after the earthquake rupture time. The difference between trough and cusp amounts to almost 4 m. A second wave arrived after approximately 13 minutes with a preceding trough at 12 minutes.

The corresponding synthetic time series derived from the tsunami scenario is also shown in Fig. 10. Although a leading wave trough is not present in the scenario results, the magnitude of the wave is well captured. Note, that the initial negative shift of approx. -80 cm within the first minute of the scenario is a modeling artefact that we explain hereafter in Sec. 5.3. It cannot be easily filtered out, due to re-adjustments throughout the computation to the background mean sea level. After 5 min of simulated time, the model mareogram resembles the measured wave behavior, characterized by a dominant wave period of about 4 min. The scenario exposes a clear resonating wave behavior due to the narrow geometry of the Bay. We note that these wave amplitudes are reproduced due to displacements resulting from the earthquake, without any contribution from landsliding.

Fig. 11 displays the maximum run-up obtained from the tsunami scenario at locations where observations have been reported around the Bay. We consider only those points on land that are reached by water in the scenario. A quantitative view comparing these same results with observations is shown in Fig. 12. The overall agreement is quite remarkable, with some overestimation of

the run-up in the northern margins of the bay and some slight underestimation in the southern part near Grandmall Palu City. In general, errors are lower than 10%. What we can conclude is that large misfit in the run-up heights are more or less randomly distributed, suggesting local amplification effects that cannot be captured in the scenario due to insufficient bathymetry/topography resolution. Fig. 13 shows maximum inundation depths computed from the tsunami scenario near Palu City. Qualitatively, the results from the scenario agree quite well with observations, as the largest inundation depths are close to the Grandmall area, where vast damage due to the tsunami was reported.

In summary, the tsunami scenario sourced by coseismic displacements from the dynamic earthquake rupture scenario yields results that are qualitatively comparable to available observations. Wave amplitudes match well, as do the run-up distribution and the inundation distances, given the limited quality of the available topography data.

## 5 Discussion

The Palu, Sulawesi tsunami was as unexpected as it was devastating. While the Palu-Koro fault system was known as a very active strike-slip plate boundary tsunamis from strike-slip events are generally not anticipated. Fears arise that other regions, currently not expected to sustain tsunami-triggering ruptures, are at risk. The here presented physics-based, coupled earthquake-tsunami model shows that a submarine strike-slip fault can produce a tsunami, if a component of dip-slip faulting occurs. In the following, we discuss advantages and limitations of physics-based models of tsunamigenesis as well as of the earthquake and tsunami model individually. We then focus on the broader implications of rapid coupled scenarios for seismic hazard mitigation and response. Finally, we look ahead to improving the here presented coupled model in light of newly available information and data.

### 5.1 Success and limitation of the physics-based tsunami source

We constrain the initial conditions for our coupled model according to the available earthquake data and physical constraints provided by previous studies, including those reporting regional transtension (Walpersdorf et al, 1998; Socquet et al, 2006; Bellier et al, 2006). A stress field characterized by transtension induces a normal component of slip on the dipping faults in the earthquake scenario. The here assumed degree of transtension

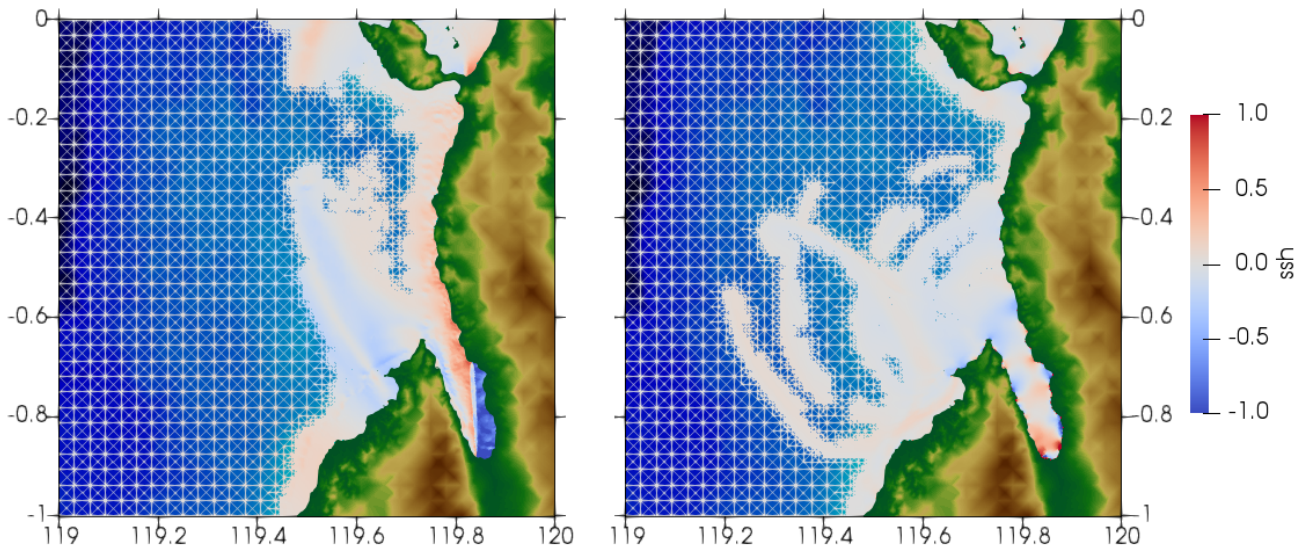


**Fig. 8** Snapshots of the tsunami simulation at 20 s (left) and 600 s (right), showing the dynamic mesh adaptivity of the simulation.

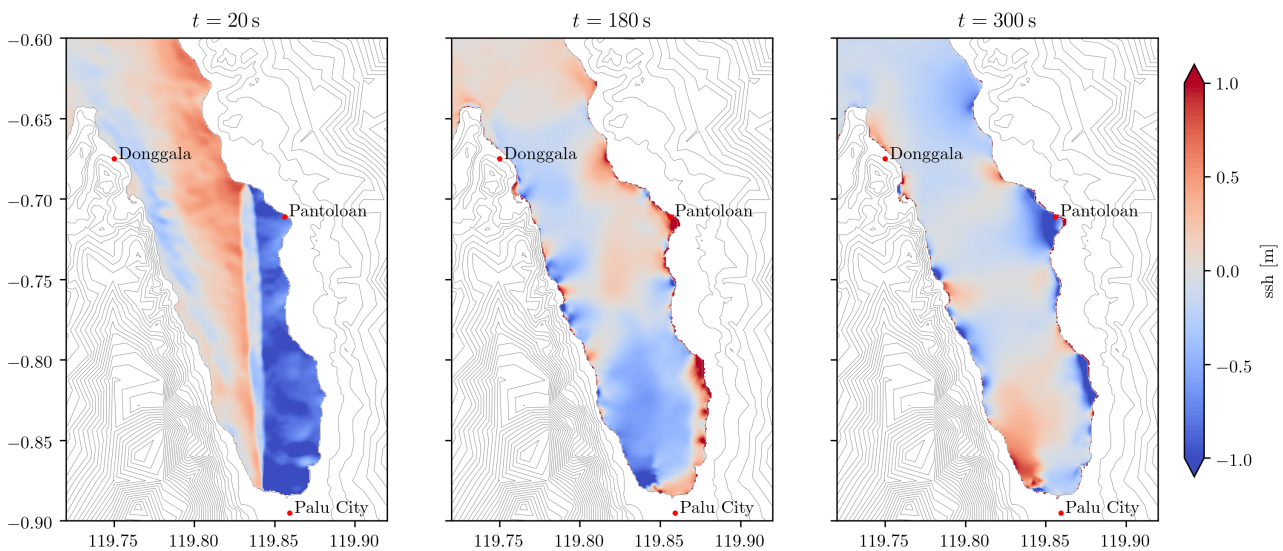


**Fig. 9** Snapshots of the tsunami simulation at 20 s, 180 s and 300 s (left to right), showing only the area of Palu Bay.

848 translates into a fault slip rake of about  $15^\circ$  on the  $65^\circ$   
 849 dipping modeled faults (Fig. 4c), which is consistent with  
 850 the earthquake focal mechanism (USGS, 2018a).

851 The such induced normal slip component results in  
 852 widespread uplift and subsidence. Fault surface ruptur-  
 853 ing generates a step in the bathymetry across the fault  
 854 of 1.5 m in average within Palu Bay, which translates  
 855 into a step in the bathymetry perturbation of similar  
 856 magnitude. (Fig. 7c). This is sufficient for triggering  
 857 a realistic tsunami that reproduces the observational  
 858 data quite well. In particular it is enough to obtain the  
 859 observed wave amplitude at the Pantoloan harbor wave  
 860 gauge and the recorded run-up heights.

861 However, we point out that transtension is not an  
 862 indispensable condition to generate oblique faulting in  
 863 such a fault network. From static considerations, we  
 864 indeed infer that specific alternative stress orientations  
 865 can equally induce a considerable dip-slip component in  
 866 biaxial stress regimes (Fig. S3).

867 The coupled earthquake model performs well at re-  
 868 producing observations from a macroscopic perspective  
 869 and suggests that additional sources of tsunami gener-  
 870 ation are not needed to explain the tsunami. However,  
 871 it does not constrain the small-scale features of the  
 872 tsunami source and thus does not allow to completely



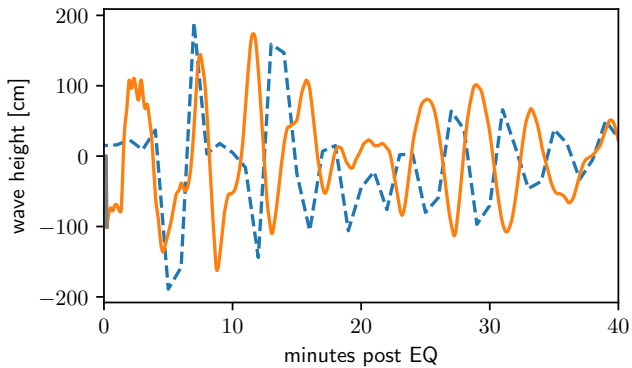


**Fig. 10** Time series from the wave gauge at Pantoloan port. Blue dashed: measurements, orange: output from the model scenario.

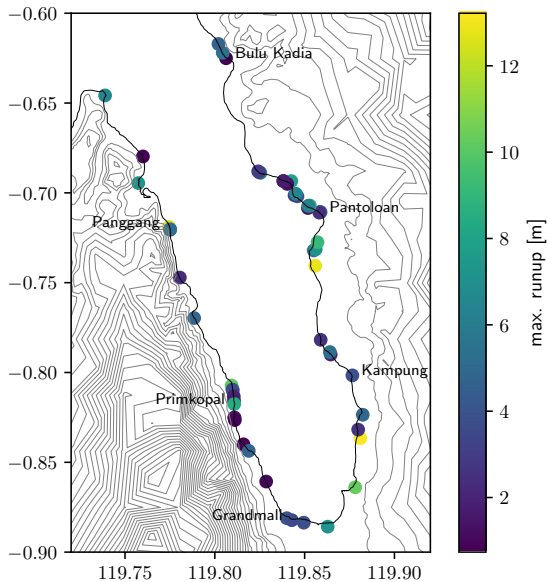


**Fig. 11** Maximum simulated run-up at different locations around Palu Bay, where observations have been recorded.

873 rule out other, potentially additional, sources of tsunami  
874 generation.

875 For example, despite the overall consistency of the  
876 earthquake scenario results with data, the fault within  
877 the Bay may have hosted a different or more compli-  
878 cated slip profile than this scenario produces. The fault  
879 geometry underneath the Bay is not known. We here  
880 choose a simple geometry that honors the information  
881 at hand (see Sec. 3.2.2). However, complex faulting may  
882 also exist there, as observed south of the Bay where slip  
883 partitioning between minor dip-slip fault strands and  
884 the primary rupture occurred (Socquet et al, 2019). Fur-  
885 thermore, a less smooth fault geometry in the Northern  
886 region, closely fitting inferred fault traces, may allow

887 reducing fault slip locally, and therefore better fitting  
888 ground displacement observations in the North.

889 Finally, incorporating the effect of landslides is likely  
890 to be necessary to capture local features of the tsunami  
891 wave and inundation patterns. Constraining these sources  
892 is very difficult without pre- and post-event high-resolution  
893 bathymetric charts. Our study suggests that these sources  
894 play a secondary role in explaining the overall tsunami  
895 magnitude and wave patterns, since these can be gener-  
896 ated by strike-slip faulting with a normal slip compo-  
897 nent.

## 5.2 The Sulawesi earthquake scenario 898

899 The speed of this earthquake is of utmost interest, al-  
900 though it does not provide an important contribution  
901 to the tsunami generation in this scenario. We review  
902 our results here and note avenues for additional mod-  
903 eling. The initial stress state and lithology included in  
904 the physical earthquake model are areas that could be  
905 improved with more in-depth study and better available  
906 data.

907 The dynamic earthquake model requires supershear  
908 rupture velocities to produce results that agree with the  
909 teleseismic data and moment rate function. This scenario  
910 also provides new perspectives on the possible timing  
911 and mechanism of this supershear rupture. Bao et al  
912 (2019) infer an average rupture velocity of about 4 km/s  
913 from back-projection. This speed corresponds to a barely  
914 stable mechanical regime, which is interpreted as being  
915 promoted by a damage zone around the mature Palu-  
916 Koro fault that formed during previous earthquakes.

917 In contrast, our earthquake scenario features an early  
918 and persistent rupture velocity of 5 km/s on average,  
919 close to P-wave speed. Supershear rupture speed is en-  
920 abled in our model by a relatively low fault strength  
921 and triggered immediately at rupture onset by a highly  
922 overstressed nucleation patch. Supershear transition is  
923 enabled and enhanced by high background stresses (or  
924 more generally, low ratios of strength excess over stress  
925 drop) (Andrews, 1976). The so called transition distance,  
926 the rupture propagation distance at which supershear  
927 rupture starts to occur, also depends on nucleation  
928 energy (Dunham, 2007; Gabriel et al, 2012, 2013). Ob-  
929 servational support for the existence of a highly stressed  
930 nucleation region arises from the series of foreshocks  
931 that occurred nearby in the days before the mainshock,  
932 including a  $M_w$  6.1 on the same day of the mainshock.

933 We conducted numerical experiments reducing the  
934 level of overstress within the nucleation patch, reach-  
935 ing a critical overstress level at which supershear is not  
936 anymore triggered immediately at rupture onset. These

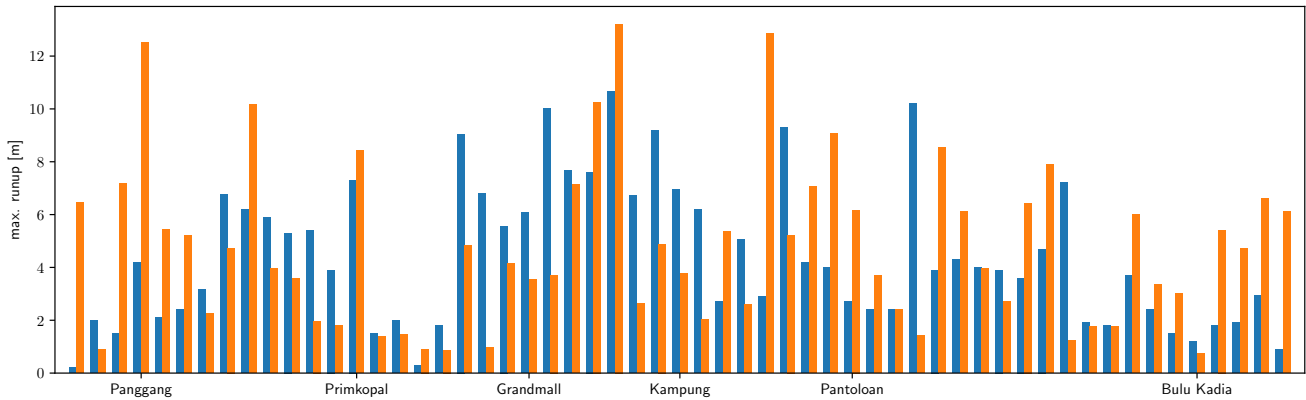


**Fig. 12** Maximum run-up from observations (blue) and simulation (orange) at different locations around Palu Bay (left to right: around the Bay from the northwest to the south to the northeast, see Fig. 11 for locations).

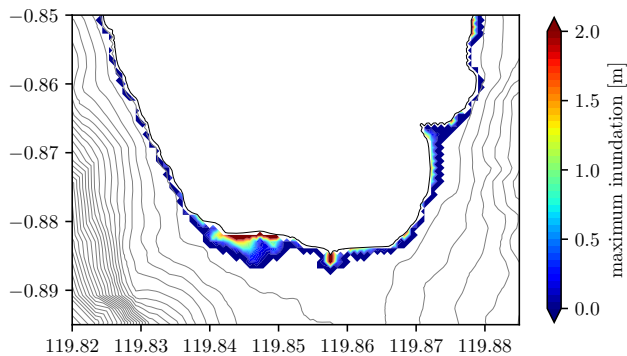


**Fig. 13** Maximum inundation computed from the tsunami scenario near Palu City.

937 alternative models initiate at subshear rupture speeds  
 938 and never transition to supershear. Importantly, these  
 939 slower earthquake scenarios do not reproduce our obser-  
 940 vational constraints, specifically teleseismic waveforms  
 941 and moment release rate.

942 Stress and/or strength variations due, for example,  
 943 to variations in tectonic loading, stress release by pre-  
 944 vious earthquakes, or local material heterogeneities are  
 945 expected, but poorly constrained and therefore not in-  
 946 cluded in our dynamic rupture model. Accounting for  
 947 such features in relation to long term deformation can  
 948 distinctly influence the stress field and lithological con-  
 949 trasts (e.g., van Dinther et al, 2013; Dal Zilio et al, 2018,  
 950 2019; Preuss et al, 2019; D’Acquisto et al, 2018; van  
 951 Zelst et al, 2019). Realistic initial conditions in terms  
 952 of stress and lithology are shown to significantly influ-  
 953 ence the dynamics of individual ruptures (Lotto et al,  
 954 2017a; van Zelst et al, 2019). Specifically, different fault  
 955 stress states for the Palu and the Northern fault seg-  
 956 ments are possible, since the Palu-Koro fault acts as

957 the regional plate-bounding fault that likely experiences  
 958 increased tectonic loading (Fig. 1a). The introduction of  
 959 self-consistent, physics-based stress and strength states  
 960 could be obtained by coupling this earthquake-tsunami  
 961 framework to geodynamic seismic cycle models (e.g.,  
 962 van Dinther et al, 2013, 2014), as done in Gabriel et al  
 963 (2018). However, in light of an absence of data or models  
 964 justifying the introduction of complexity, we here use  
 965 the simplest option with a laterally homogeneous stress  
 966 field that honors the regional scale transtension.

967 We also note that the earthquake scenario is depen-  
 968 dent on the subsurface structure model (e.g., Lotto et al,  
 969 2017a; van Zelst et al, 2019). The local velocity model  
 970 of Awaliah et al (2018) is of limited resolution within  
 971 the Palu area, since only one of the used stations allows  
 972 illuminating this region. Despite the strong effects of  
 973 data regularization, this is to our knowledge the most  
 974 detailed data set characterizing the subsurface in the  
 975 area of study.

### 5.3 The Sulawesi tsunami scenario 976

977 Overall, the tsunami model shows good agreement with  
 978 available key observations. Wave amplitudes and peri-  
 979 ods at the only available tide gauge station in the Bay  
 980 match well. Run-up and inundation data from our model  
 981 show satisfactory agreement with the observations by  
 982 international survey teams (Yalciner et al, 2018).

983 Apart from the above discussed earthquake model  
 984 limitations that may influence the tsunami characteris-  
 985 tics, the following additional reasons may cause devia-  
 986 tions to tsunami observations: (a) insufficiently accurate  
 987 bathymetry/topography data; (b) simplified coupling  
 988 between earthquake rupture and tsunami scenarios; (c)  
 989 approximation by hydrostatic shallow water wave theory.  
 990 In the following we will briefly discuss these topics.

The insufficient resolution of the bathymetry and topography datasets may prevent us from properly capturing local effects, which may dominate some tsunami and inundation observations. In fact, subtle features such as a wall or dam, a small inlet of a few meters width, rocks or submarine obstacles can strongly modulate the water wave locally. These effects cannot be accounted for in our computation based on a relatively coarse bathymetry/topography data set of about 190 m resolution.

The accuracy of the tsunami model may also be affected by the simplification underlying the shallow water equations. In particular, a near-field tsunami within a narrow bay may be affected by large bathymetry gradients. In the shallow-water framework, all three spatial components of the ground displacements generated by the earthquake model cannot be properly accounted for. In fact, a direct application of a horizontal displacement to the hydrostatic (single layer) shallow water model would lead to unrealistic momentum in the whole water column. Additionally, all bottom movements are immediately and directly transferred to the whole water column, since we model the water wave by (essentially 2D) shallow water theory. In reality, an adjustment process takes place. The large bathymetry gradients may also lead to non-hydrostatic effects in the water column, which cannot be neglected. Suitable numerical discretizations are underway (e.g., Jeschke et al, 2017), and should be tested to quantify the influence of such effects in realistic situations such as the Sulawesi event.

We account for the effect of the horizontal seafloor displacements by applying the method proposed by Tanioka and Satake (1996). We observe only minor differences in the modeled water waves when including the effect of the horizontal ground displacements (see Fig. 9, 13, S7 and S8). We thus conclude that vertical ground displacements are the primary cause of the tsunami.

A modeling artefact is visible in the synthetic mareogram at Pantoloan wave gauge, directly after the earthquake (Fig. 10). About 80 cm of ground subsidence is imprinted on the synthetic data, but not visible in the observed signal. This is the direct effect of the subsidence at Pantoloan (cf. Fig. 7 and Fig. S2). We cannot remove this shift from the time series, since the tsunami model includes a background mean sea level, to which it readjusts throughout the computation. On the other hand, the tide gauge at Pantoloan is not sensitive to a possible uplift or subsidence at that site. In fact, the instrument and the water surface are displaced jointly during an earthquake, and therefore the distance between them remains fixed.

#### 5.4 Advantages and outcome of a physics-based coupled model

By capturing dynamic slip evolution that is consistent with the fault geometry and the regional stress field, the dynamic rupture model produces mechanically consistent ground deformation, even in submarine areas where space borne imaging techniques are blind. These seafloor displacement time-histories, which include the influence of seismic waves, in nature contribute to source the tsunami and are utilized as such in this coupled framework. However, the earthquake-tsunami coupling is not physically seamless. For example, as noted above, seismic waves cannot be captured using the shallow water approach, but rather require a non-hydrostatic water body (e.g. Lotto et al, 2018). However, the coupled system remains mechanically consistent to the order of the typical spatio-temporal scales governing tsunami modeling. Thus, a physics-based, coupled model is well-posed to shed light on the mechanisms and competing hypotheses governing earthquake-tsunami sequences as puzzling as the Sulawesi event.

The use of a dynamic rupture earthquake source has distinct contributions relative to the standard finite-fault inversion source approach, which is typically used in tsunami models. The latter enables close fitting of observations through the use of a large number of free parameters. Despite recent advances (e.g., Shimizu et al, 2019), kinematic models typically need to pre-define fault geometries. Naive first-order finite-fault sources are automatically determined after an earthquake and this can be done quickly (e.g. by USGS or GFZ German Research Centre for Geoscience), which is a great advantage. Models can be improved later on by including new data and more complexity. However, kinematic models are characterized by inherent non-uniqueness and do not ensure mechanical consistency of the source (e.g., Mai et al, 2016). The physics-based model also suffers from non-uniqueness, but this is reduced, since it excludes scenarios that are not mechanically viable.

These advantages and the demonstrated progress potentially make physics-based, coupled earthquake-tsunami modeling an important tool for seismic hazard mitigation and rapid earthquake response. We facilitate rapid modeling of the earthquake scenario by systematically defining a suitable parameterization for the regional and fault-specific characteristics. We use a pre-established, efficient algorithm, based on physical relationships between parameters, to assign the ill-constrained stress state and strength on the fault using a few trial simulations (Ulrich et al, 2019). This limits the required input parameters to subsurface structure, fault structure, and four parameters governing the

stress state and fault conditions. This enables rapid response in delivering physics-driven interpretations that can be integrated synergistically with established data-driven efforts within the first days and weeks after an earthquake.

## 5.5 Looking forward

The coupled model presented here produces a realistic scenario that agrees with key characteristics of available earthquake and tsunami data. However, future efforts will be directed toward improving our model as new information on fault structure or displacements within the Bay or additional tide gauge measurements become available.

In addition, different earthquake models varying in their fault geometry or in the physical laws governing on- and off-fault behavior can be utilized in further studies of the influence of earthquake characteristics on tsunami generation and impact.

Our model provides high resolution synthetics of, e.g., ground deformation in space and time. These predictions can be readily compared to observational data yet to be made available to the scientific community. We provide this in Appendix Sec. 8.2.

Spatial variations of regional stress and fault strength could be constrained in the future by tectonic seismic cycle modeling capable of handling complex fault geometries. Future dynamic earthquake rupture modeling may additionally explore how varying levels of preexisting and coseismic off-fault damage affect the rupture speed specifically and rupture dynamics in general.

Future research should also be directed towards an even more realistic coupling strategy together with an extended sensitivity analysis on the effects of such coupling. This, e.g., requires the integration of non-hydrostatic extensions for the tsunami modeling part (Jeschke et al, 2017) into the ASCETE coupling framework .

## 6 Conclusions

We present a coupled, physics-based scenario of the 2018 Palu, Sulawesi earthquake and tsunami, which is constrained by rapidly available observations. We demonstrate that coseismic oblique-slip on a dipping strike-slip fault produces a vertical step across the submarine fault segment of 1.5 m on average in the tsunami source. This is sufficient to produce reasonable tsunami amplitude and wave run-up. The critical normal-faulting component results from transtension, prevailing in this region, and the fault system geometry.

The fully dynamic earthquake model captures important features, including the timing and speed of the rupture, 3D geometric complexities of the faults, and the influence of seismic waves on the rupture propagation. We find that an early-onset of supershear rupture speed, sustained for the duration of the rupture across geometric complexities, is required to match a range of far-field and near-fault observations.

The modelled tsunami amplitudes and wave run-ups agree with observations within the range of modeling uncertainties dominated by the available bathymetry and topography data. We conclude that the primary tsunami source may have been coseismically generated vertical displacements. However, in a holistic approach aiming to match high-frequency tsunami features, local effects such as landsliding, non-hydrostatic wave effects, and high resolution topographical features should be included.

The coupling of physics-based models, as tackled within the ASCETE framework, is specifically useful to assess tsunami hazard in tectonic settings currently underrepresented in operational hazard assessment. We demonstrate that high-performance computing empowered dynamic rupture modeling produces well-constrained studies integrating source observations and earthquake physics very quickly after an event occurs. In the future, such physics-based earthquake-tsunami response can complement both on-going hazard mitigation and the established urgent response tool set.

## 7 Acknowledgements

We thank Taufiqurrahman for helping us accessing data on Indonesian websites, and for putting us in contact with Indonesian researchers. We thank Dr. T. Yudistira for providing their crustal velocity model of Sulawesi and Dr. Andreas Fichtner for providing us a chunk of their ‘Collaborative seismic earth model’. We thank Dr. Marcello de Michele for providing his inferred ground-deformations data and for fruitful discussions. The ALOS-2 original data are copyright JAXA and provided under JAXA RA6 PI projects P3278 and P3360. Dr. Widodo S. Pranowo provided access to very early field survey observations. Furthermore, Dr. Abdul Muhari supported this work by providing 1-minute tide gauge data for the Pantoloan tide gauge. Finally we thank the participant of the AGU special session about the Palu earthquake for interesting discussions.

The work presented in this paper was enabled by the Volkswagen Foundation (project ‘ASCETE’, grant no. 88479).

Computing resources were provided by the Institute of Geophysics of LMU Munich (Oeser et al, 2006),



the Leibniz Supercomputing Centre (LRZ, projects no. h019z, pr63qo, and pr45fi on SuperMUC), and the Center for Earth System Research and Sustainability (CEN) at University of Hamburg.

T.U., E.H.M. and A.-A.G. acknowledge support by the German Research Foundation (DFG) (projects no. KA 2281/4-1, GA 2465/2-1, GA 2465/3-1), by BaCaTec (project no. A4) and BayLat, by KONWIHR – the Bavarian Competence Network for Technical and Scientific High Performance Computing (project NewWave), by KAUST-CRG (GAST, grant no. ORS-2016-CRG5-3027 and FRAGEN, grant no. ORS-2017-CRG6 3389.02), by the European Union’s Horizon 2020 research and innovation program (ExaHyPE, grant no. 671698 and ChEESE, grant no. 823844).

S.V. acknowledges support by Einstein Stiftung Berlin through grant EVF-2017-358(FU).

Part of this research was performed at the Jet Propulsion Laboratory, California Institute of Technology under contract with the National Aeronautics and Space Administration (NASA) by Earth Surface and Interior focus area and NISAR Science Team.

## References

Andrews D (1976) Rupture velocity of plane strain shear cracks. *Journal of Geophysical Research* 81(32):5679–5687, DOI 10.1029/JB081i032p05679

Aochi H, Madariaga R (2003) The 1999 Izmit, Turkey, earthquake: Nonplanar fault structure, dynamic rupture process, and strong ground motion. *Bulletin of the Seismological Society of America* 93(3):1249–1266, DOI 10.1785/0120020167

Argus DF, Gordon RG, DeMets C (2011) Geologically current motion of 56 plates relative to the no-net-rotation reference frame. *Geochemistry, Geophysics, Geosystems* 12(11), DOI 10.1029/2011GC003751

Awaliah WO, Yudistira T, Nugraha AD (2018) Identification of 3-d shear wave velocity structure beneath sulawesi island using ambient noise tomography method. In: 10th ACES International Workshop, URL [http://quaketm.bosai.go.jp/~shiqing/ACES2018/abstracts/aces\\_abstract\\_awaliah.pdf](http://quaketm.bosai.go.jp/~shiqing/ACES2018/abstracts/aces_abstract_awaliah.pdf)

Bao H, Ampuero JP, Meng L, Fielding EJ, Liang C, Milliner CWD, Feng T, Huang H (2019) Early and persistent supershear rupture of the 2018 magnitude 7.5 Palu earthquake. *Nature Geoscience* DOI 10.1038/s41561-018-0297-z

Bauer A, Scheipl F, Küchenhoff H, Gabriel AA (2017) Modeling spatio-temporal earthquake dynamics using generalized functional additive regression. In: *Proceedings of the 32nd International Workshop on Statistical Modelling*, vol 2, pp 146–149

Behrens J, Bader M (2009) Efficiency considerations in triangular adaptive mesh refinement. *Phil Trans R Soc A* 367(1907):4577–4589, DOI 10.1098/rsta.2009.0175

Behrens J, Rakowsky N, Hiller W, Handorf D, Läuter M, Pöpke J, Dethloff K (2005) amatos: Parallel adaptive mesh generator for atmospheric and oceanic simulation. *Ocean Modelling* 10(1–2):171–183, DOI 10.1016/j.ocemod.2004.06.003

Bellier O, Sébrier M, Seward D, Beaudouin T, Villeneuve M, Putranto E (2006) Fission track and fault kinematics analyses for new insight into the Late Cenozoic tectonic regime changes in West-Central Sulawesi (Indonesia). *Tectonophysics* 413(3–4):201–220, DOI 10.1016/j.tecto.2005.10.036

Bird P (2003) An updated digital model of plate boundaries. *Geochemistry, Geophysics, Geosystems* 4(3)

Borrero JC, Legg MR, Synolakis CE (2004) Tsunami sources in the southern California bight. *Geophysical Research Letters* 31:L13,211, DOI 10.1029/2004GL020078

Breuer A, Heinecke A, Rettenberger S, Bader M, Gabriel AA, Pelties C (????) In: *Supercomputing. ISC 2014. Lecture Notes in Computer Science*, vol 8488, DOI 10.1007/978-3-319-07518-1\_1

Burridge R (1973) Admissible speeds for plane-strain self-similar shear cracks with friction but lacking cohesion. *Geophysical Journal of the Royal Astronomical Society* 35(4):439–455

D’Acquisto M, Dal Zilio L, van Dinther Y, Molinari I, Gerya T, Kissling E (2018) Modelling tectonics and seismicity due to slab retreat along the northern apennines thrust belt. In: *AGU Fall Meeting 2018*, URL <https://agu.confex.com/agu/fm18/meetingapp.cgi/Paper/431867>

Dal Zilio L, van Dinther Y, Gerya T, Pranger C (2018) Seismic behaviour of mountain belts controlled by plate convergence rate. *Earth and Planetary Science Letters* 482:81–92

Dal Zilio L, van Dinther Y, Gerya T, Avouac J (2019) Bimodal seismicity in the Himalaya controlled by fault friction and geometry. *Nature Communications* 10:48

De Michele M (2018) URL [https://www.esa.int/spaceinimages/Images/2018/10/Indonesia\\_earthquake\\_displacement\\_data](https://www.esa.int/spaceinimages/Images/2018/10/Indonesia_earthquake_displacement_data)

DEMNAS (2018) DEMNAS – seamless digital elevation model (DEM) dan batimetri nasional. Badan Informasi Geospasial, URL <http://tides.big.go.id/DEMNAS>

Di Toro G, Han R, Hirose T, De Paola N, Nielsen S, Mizoguchi K, Ferri F, Cocco M, Shimamoto T (2011) Fault lubrication during earthquakes. *Nature* 471(7339):494–498, DOI 10.1038/nature09838

van Dinther Y, Gerya T, Dalguer L, Mai P, Morra G, Giardini D (2013) The seismic cycle at subduction thrusts: insights from seismo-thermo-mechanical models. *Journal Geophysical Research* 118:6183–6202, DOI 10.1002/2013JB010380

van Dinther Y, Mai PM, Dalguer LA, Gerya TV (2014) Modeling the seismic cycle in subduction zones: the role and spatiotemporal occurrence of off-megathrust events. *Geophysical Research Letters* 41(4):1194–1201

van Dongeren A, Vatvani D, van Ormondt M (2018) Simulation of 2018 tsunami along the coastal areas in the palu bay. In: *AGU Fall Meeting 2018*, URL <https://agu.confex.com/agu/fm18/meetingapp.cgi/Session/66627>

Dumbser M, Käser M (2006) An arbitrary high-order discontinuous Galerkin method for elastic waves on unstructured meshes – II. the three-dimensional isotropic case. *Geophysical Journal International* 167(1):319–336, DOI 10.1111/j.1365-246X.2006.03120.x

Dunham EM (2007) Conditions governing the occurrence of supershear ruptures under slip-weakening friction. *Journal of Geophysical Research: Solid Earth* 112(B7)

Dunham EM, Belanger D, Cong L, Kozdon JE (2011) Earthquake Ruptures with Strongly Rate-Weakening Friction and Off-Fault Plasticity, Part 1: Planar Faults. *Bulletin of the Seismological Society of America* 101(5):2296–2307, DOI 10.1785/0120100075, URL <https://pubs.geoscienceworld.org/bssa/article/101/5/2296-2307/326473>

- Fichtner A, van Herwaarden DP, Afanasiev M, Simute S, Krischer L, Cubuk-Sabuncu Y, Taymaz T, Colli L, Saygin E, Villasenor A, Trampert J, Cupillard P, Bunge HP, Igel H (2018) The Collaborative Seismic Earth Model: Generation 1. *Geophysical Research Letters* 45(9):4007–4016, DOI 10.1029/2018GL077338
- Gabriel AA, Ampuero JP, Dalguer LA, Mai PM (2012) The transition of dynamic rupture styles in elastic media under velocity-weakening friction. *Journal of Geophysical Research: Solid Earth* 117(B9)
- Gabriel AA, Ampuero JP, Dalguer LA, Mai PM (2013) Source properties of dynamic rupture pulses with off-fault plasticity. *Journal of Geophysical Research: Solid Earth* 118(8):4117–4126, DOI 10.1002/jgrb.50213, URL <http://onlinelibrary.wiley.com/doi/10.1002/jgrb.50213/abstract>
- Gabriel AA, Behrens J, Bader M, van Dinther Y, Gunawan T, Madden EH, Rannabauer L, Rettenberger S, Ulrich T, Uphoff C, Vater S, Wollherr S, van Zelst I (2018) S21E-0492: Coupled seismic cycle - Earthquake dynamic rupture - Tsunami models. In: AGU Fall Meeting 2018, Washington, D.C., URL <https://agu.confex.com/agu/fm18/meetingapp.cgi/Paper/453669>
- GEBCO (2015) The GEBCO 2014 Grid, version 20150318
- Harig S, Chaeroni, Pranowo WS, Behrens J (2008) Tsunami simulations on several scales: Comparison of approaches with unstructured meshes and nested grids. *Ocean Dynamics* 58:429–440
- Harris RA, Barall M, Andrews D, Duan B, Ma S, Dunham E, Gabriel AA, Kaneko Y, Kase Y, Aagaard B, et al (2011) Verifying a computational method for predicting extreme ground motion. *Seismological Research Letters* 82(5):638–644
- Harris RA, Barall M, Aagaard B, Ma S, Roten D, Olsen K, Duan B, Liu D, Luo B, Bai K, et al (2018) A suite of exercises for verifying dynamic earthquake rupture codes. *Seismological Research Letters* 89(3):1146–1162
- Heidarzadeh M, Muhari A, Wijanarto AB (2018) Insights on the source of the 28 september 2018 Sulawesi tsunami, Indonesia based on spectral analyses and numerical simulations. *Pure and Applied Geophysics* DOI 10.1007/s00024-018-2065-9
- Heidbach O, Rajabi M, Cui X, Fuchs K, Müller B, Reinecker J, Reiter K, Tingay M, Wenzel F, Xie F, Ziegler MO, Zoback ML, Zoback M (2018) The World Stress Map database release 2016: Crustal stress pattern across scales. *Tectonophysics* 744:484–498, DOI 10.1016/J.TECTO.2018.07.007
- Heinecke A, Breuer A, Rettenberger S, Bader M, Gabriel AA, Pelties C, Bode A, Barth W, Liao XK, Vaidyanathan K, Smelyanskiy M, Dubey P (2014) Petascale high order dynamic rupture earthquake simulations on heterogeneous supercomputers. In: SC14: International conference for high performance computing, networking, storage and analysis, IEEE, pp 3–14, DOI 10.1109/SC.2014.6
- IPGP (2018) URL <http://geoscope.ipgp.fr/index.php/en/catalog/earthquake-description?seis=us1000h3p4>
- Jeschke A, Pedersen GK, Vater S, Behrens J (2017) Depth-averaged non-hydrostatic extension for shallow water equations with quadratic vertical pressure profile: Equivalence to Boussinesq-type equations. *International Journal for Numerical Methods in Fluids* 84(10):569–583, DOI 10.1002/flid.4361
- Krischer L, Hutko AR, van Driel M, Stähler S, Bahavar M, Trabant C, Nissen-Meyer T (2017) On-demand custom broadband synthetic seismograms. *Seismological Research Letters* 88(4):1127–1140, DOI 10.1785/0220160210
- Legg MR, Borrero JC (2001) Tsunami potential of major restraining bends along submarine strike-slip faults. In: *Proceedings of the International Tsunami Symposium 2001*, NOAA/PMEL, 1, pp 331–342
- Legg MR, Borrero JC, Synolakis CE (2003) Tsunami hazards from strike-slip earthquakes. *American Geophysical Union, Fall Meeting 2003*, abstract id OS21D-06 URL <http://adsabs.harvard.edu/abs/2003AGUFMOS21D..06L>
- Liang C, Fielding EJ (2017) Interferometry with ALOS-2 full-aperture ScanSAR data. *IEEE Transactions on Geoscience and Remote Sensing* 55(5):2739–2750
- Liang Q, Marche F (2009) Numerical resolution of well-balanced shallow water equations with complex source terms. *Advances in Water Resources* 32:873–884, DOI 10.1016/j.advwatres.2009.02.010
- Liu PLF, Barranco I, Fritz HM, Haase JS, Prasetya GS, Qiu Q, Sepulveda I, Synolakis C, Xu X (2018) What we do and don't know about the 2018 Palu Tsunami – A future plan. In: AGU Fall Meeting 2018, URL <https://agu.confex.com/agu/fm18/meetingapp.cgi/Paper/476669>
- Lotto GC, Dunham EM, Jeppson TN, Tobin HJ (2017a) The effect of compliant prisms on subduction zone earthquakes and tsunamis. *Earth and Planetary Science Letters* 458:213–222
- Lotto GC, Nava G, Dunham EM (2017b) Should tsunami simulations include a nonzero initial horizontal velocity? *Earth, Planets and Space* 69(1):117
- Lotto GC, Jeppson TN, Dunham EM (2018) Fully coupled simulations of megathrust earthquakes and tsunamis in the Japan trench, Nankai trough, and Cascadia subduction zone. *Pure and Applied Geophysics* pp 1–33
- Løvholt F, Hasan H, Lorito S, Romano F, Brizuela B, Piatanesi A, Pedersen GK (2018) Multiple source sensitivity study to model the 28 September Sulawesi tsunami – landslide and strike slip sources. In: AGU Fall Meeting 2018, Washington, DC, URL <https://agu.confex.com/agu/fm18/meetingapp.cgi/Paper/476627>
- Mai PM (2019) Supershear tsunami disaster. *Nature Geoscience* pp 7–8, DOI 10.1038/s41561-019-0308-8
- Mai PM, Schorlemmer D, Page M, Ampuero JP, Asano K, Causse M, Custodio S, Fan W, Festa G, Galis M, et al (2016) The earthquake-source inversion validation (SIV) project. *Seismological Research Letters* 87(3):690–708
- Mansinha L, Smylie DE (1971) The displacement fields of inclined faults. *Bull Seis Soc Am* 61(5):1433–1440
- Muhari A, Imamura F, Arikawa T, Hakim AR, Afriyanto B (2018) Solving the puzzle of the September 2018 Palu, Indonesia, tsunami mystery: Clues from the tsunami waveform and the initial field survey data. *Journal of Disaster Research* 13:sc20181,108, DOI 10.20965/jdr.2018.sc20181108
- Oeser J, Bunge HP, Mohr M (2006) Cluster design in the earth sciences: Tethys. In: *International conference on high performance computing and communications*, Springer, pp 31–40
- Okada Y (1985) Surface deformation due to shear and tensile faults in a half-space. *Bulletin of the Seismological Society of America* 75(4):1135
- Okuwaki R, Yagi Y, Shimizu K (2018) rokuwaki/2018paluindonesia: v2.0. DOI 10.5281/zenodo.1469007
- Pelinovsky E, Yuliadi D, Prasetya G, Hidayat R (1997) The 1996 Sulawesi Tsunami. *Natural Hazards* 16(1):29–38, DOI 10.1023/A:1007904610680
- Pelties C, Puente J, Ampuero JP, Brietzke GB, Käser M (2012) Three-dimensional dynamic rupture simulation with a high-order discontinuous Galerkin method on unstruc-

- 1445 tured tetrahedral meshes. *Journal of Geophysical Research: Solid Earth* 117(B2) 1446
- 1447 Pelties C, Gabriel AA, Ampuero JP (2013) Verification of an ader-dg method for complex dynamic rupture problems. *Geoscientific Model Development Discussions* 6:5981–6034 1448
- 1449 Pelties C, Gabriel AA, Ampuero JP (2014) Verification of an ADER-DG method for complex dynamic rupture problems. *Geoscientific Model Development* 7(3):847–866, DOI 10.5194/gmd-7-847-2014 1450
- 1451 Power W, Clark K, King DN, Borrero J, Howarth J, Lane EM, Goring D, Goff J, Chagué-Goff C, Williams J, Reid C, Whittaker C, Mueller C, Williams S, Hughes MW, Hoyle J, Bind J, Strong D, Litchfield N, Benson A (2017) Tsunami runup and tide-gauge observations from the 14 november 2016 m7.8 kaikōura earthquake, new zealand. *Pure and Applied Geophysics* 174(7):2457–2473, DOI 10.1007/s00024-017-1566-2 1452
- 1453 Prasetya GS, De Lange WP, Healy TR (2001) The Makassar Strait Tsunamigenic region, Indonesia. *Natural Hazards* 24(3):295–307, DOI 10.1023/A:1012297413280 1454
- 1455 Preuss S, Herrend-Áurfer R, Gerya T, Ampuero J, van Dinther Y (2019) Seismic and aseismic fault growth lead to different fault orientations. DOI 10.31223/osf.io/an92e 1456
- 1457 de la Puente J, Ampuero JP, Käser M (2009) Dynamic rupture modeling on unstructured meshes using a discontinuous Galerkin method. *Journal of Geophysical Research: Solid Earth* 114(B10) 1458
- 1459 Quantum G (2013) Development team.(2013). quantum gis geographic information system. open source geospatial foundation project 1460
- 1461 Rettenberger S, Meister O, Bader M, Gabriel AA (2016) Asagi: A parallel server for adaptive geoinformation. In: *Proceedings of the Exascale Applications and Software Conference 2016*, ACM, New York, NY, USA, EASC '16, pp 2:1–2:9, DOI 10.1145/2938615.2938618 1462
- 1463 Rosen PA, Gurrola E, Sacco GF, Zebker H (2012) The insar scientific computing environment. In: *Synthetic Aperture Radar, 2012. EUSAR. 9th European Conference on, VDE*, pp 730–733 1464
- 1465 Ryan KJ, Geist EL, Barall M, Oglesby DD (2015) Dynamic models of an earthquake and tsunami offshore Ventura, California. *Geophysical Research Letters* 42(16):6599–6606, DOI 10.1002/2015GL064507 1466
- 1467 Sassa S, Takagawa T (2019) Liquefied gravity flow-induced tsunami: first evidence and comparison from the 2018 indonesia sulawesi earthquake and tsunami disasters. *Landslides* 16(1):195–200, DOI 10.1007/s10346-018-1114-x 1468
- 1469 SeisSol github (2019) Seissol github. URL <https://github.com/SeisSol/SeisSol> 1470
- 1471 SeisSol website (2019) Seissol website. URL [www.seissol.org](http://www.seissol.org) 1472
- 1473 Sepulveda I, Haase JS, Liu PLF, Xu X, Carvajal M (2018) On the contribution of co-seismic displacements to the 2018 palu tsunami. In: *AGU Fall Meeting 2018*, URL <https://agu.confex.com/agu/fm18/meetingapp.cgi/Paper/476717> 1474
- 1475 Shimizu K, Yagi Y, Okuwaki R, Fukahata Y (2019) Development of an inversion method to extract information on fault geometry from teleseismic data. DOI 10.31223/osf.io/q58t7 1476
- 1477 Simons WJ, Riva R, Pietrzak J, et al (2018) Tsunami potential of the 2018 Sulawesi earthquake from GNSS constrained source mechanism. In: *AGU Fall Meeting 2018*, Washington, D.C., URL <https://agu.confex.com/agu/fm18/meetingapp.cgi/Paper/476730> 1478
- 1479 Socquet A, Simons W, Vigny C, McCaffrey R, Subarya C, Sarsito D, Ambrosius B, Spakman W (2006) Microblock rotations and fault coupling in SE Asia triple junction (Sulawesi, Indonesia) from GPS and earthquake slip vector data. *Journal of Geophysical Research: Solid Earth* 111(B8) 1480
- 1481 Socquet A, Hollingsworth J, Pathier E, Bouchon M (2019) Evidence of supershear during the 2018 magnitude 7.5 Palu earthquake from space geodesy. *Nature Geoscience* DOI 10.1038/s41561-018-0296-0 1482
- 1483 Synolakis CE, Bernard EN, Titov VV, Kanoğlu U, González FI (2007) Standards, criteria, and procedures for NOAA evaluation of tsunami numerical models. Tech. Rep. NOAA Technical Memorandum OAR PMEL-135, NOAA/OAR/PMEL 1484
- 1485 Tanioka Y, Satake K (1996) Tsunami generation by horizontal displacement of ocean bottom. *Geophysical Research Letters* 23(8):861–864, DOI 10.1029/96GL00736 1486
- 1487 Tanioka Y, Yudhicara, Kususe T, Kathirolu S, Nishimura Y, Iwasaki SI, Satake K (2006) Rupture process of the 2004 great Sumatra-Andaman earthquake estimated from tsunami waveforms. *Earth, Planets and Space* 58(2):203–209, DOI 10.1186/BF03353379 1488
- 1489 Ulrich T, Gabriel AA, Ampuero JP, Xu W (2019) Dynamic viability of the 2016 mw 7.8 Kaikōura earthquake cascade on weak crustal faults. DOI 10.31223/osf.io/aed4b, accepted in *Nat. Comm.* 1490
- 1491 Uphoff C, Rettenberger S, Bader M, Madden E, Ulrich T, Wollherr S, Gabriel AA (2017) Extreme scale multi-physics simulations of the tsunamigenic 2004 sumatra megathrust earthquake. In: *Proceedings of the International Conference for High Performance Computing, Networking, Storage and Analysis, SC 2017*, DOI 10.1145/3126908.3126948 1492
- 1493 USGS (2018a) URL <https://earthquake.usgs.gov/earthquakes/eventpage/us1000h3p4/moment-tensor> 1494
- 1495 USGS (2018b) URL <https://earthquake.usgs.gov/earthquakes/eventpage/us1000h3p4/finite-fault> 1496
- 1497 Valkaniotis S, Ganas A, Tsironi V, Barberopoulou A (2018) A preliminary report on the M7.5 Palu 2018 earthquake co-seismic ruptures and landslides using image correlation techniques on optical satellite data. DOI 10.5281/zenodo.1467128, report submitted to EMSC 1498
- 1499 Vallée M, Charléty J, Ferreira AMG, Delouis B, Vergoz J (2011) SCARDEC: a new technique for the rapid determination of seismic moment magnitude, focal mechanism and source time functions for large earthquakes using body-wave deconvolution. *Geophysical Journal International* 184(1):338–358, DOI 10.1111/j.1365-246X.2010.04836.x 1500
- 1501 Vater S, Behrens J (2014) Well-balanced inundation modeling for shallow-water flows with Discontinuous Galerkin schemes. In: *Fuhrmann J, Ohlberger M, Rohde C (eds) Finite Volumes for Complex Applications VII – Elliptic, Parabolic and Hyperbolic Problems, Springer Proceedings in Mathematics & Statistics*, vol 78, pp 965–973, DOI 10.1007/978-3-319-05591-6\_98 1502
- 1503 Vater S, Beisiegel N, Behrens J (2015) A limiter-based well-balanced discontinuous galerkin method for shallow-water flows with wetting and drying: One-dimensional case. *Advances in Water Resources* 85:1–13, DOI 10.1016/j.advwatres.2015.08.008 1504
- 1505 Vater S, Beisiegel N, Behrens J (2017) Comparison of wetting and drying between a RKDG2 method and classical FV based second-order hydrostatic reconstruction. In: *Cancès C, Omnes P (eds) Finite Volumes for Complex Applications VIII - Hyperbolic, Elliptic and Parabolic Problems*, Springer, pp 237–245, DOI 10.1007/978-3-319-57394-6\_26 1506
- 1507 Vater S, Beisiegel N, Behrens J (2018) A limiter-based well-balanced discontinuous Galerkin method for shallow-water flows with wetting and drying: Triangular grids. <https://arxiv.org/abs/1811.09505> 1508
- 1509 Vigny C, Perfettini H, Walpersdorf A, Lemoine A, Simons W, van Loon D, Ambrosius B, Stevens C, McCaffrey R, Morgan 1510

- 1577 P, et al (2002) Migration of seismicity and earthquake  
1578 interactions monitored by gps in se asia triple junction:  
1579 Sulawesi, indonesia. *Journal of Geophysical Research: Solid*  
1580 *Earth* 107(B10):ETG-7
- 1581 Walpersdorf A, Rangin C, Vigny C (1998) GPS compared  
1582 to long-term geologic motion of the north arm of Sulawesi.  
1583 *Earth and Planetary Science Letters* 159(1):47-55, DOI  
1584 10.1016/S0012-821X(98)00056-9
- 1585 Watkinson IM, Hall R (2017) Fault systems of the eastern  
1586 indonesian triple junction: evaluation of quaternary activity  
1587 and implications for seismic hazards. *Geological Society,*  
1588 *London, Special Publications* 441(1):71-120
- 1589 Weatherall P, Marks KM, Jakobsson M, Schmitt T, Tani  
1590 S, Arndt JE, Rovere M, Chayes D, Ferrini V, Wigley R  
1591 (2015) A new digital bathymetric model of the world's  
1592 oceans. *Earth and Space Science* 2(8):331-345, DOI  
1593 10.1002/2015EA000107
- 1594 Wollherr S, Gabriel AA, Mai PM (2018a) Landers 1992  
1595 "reloaded": an integrative dynamic earthquake rupture  
1596 model. DOI 10.31223/osf.io/kh6j9, URL [eartharxiv.org/  
1597 kh6j9](https://eartharxiv.org/kh6j9)
- 1598 Wollherr S, Gabriel AA, Uphoff C (2018b) Off-fault plas-  
1599 ticity in three-dimensional dynamic rupture simulations  
1600 using a modal Discontinuous Galerkin method on unstruc-  
1601 tured meshes: implementation, verification and application.  
1602 *Geophysical Journal International* 214(3):1556-1584, DOI  
1603 10.1093/gji/ggy213
- 1604 Yalciner AC, Hidayat R, Husrin S, Prasetya G, Annunziato  
1605 A, Doğan GG, Zaytsev A, Omira R, Proietti C, Probst P,  
1606 Paparo MA, Wronna M, Pronin P, Giniyatullin A, Putra PS,  
1607 Hartanto D, Ginanjar G, Kongko W, Pelinowski E (2018)  
1608 The 28th September 2018 Palu earthquake and tsunami  
1609 ITST 07-11 November 2018 post tsunami field survey report  
1610 (short). Report, Middle East Technical University (and  
1611 others), Ankara, Turkey, URL [https://drive.google.com/  
1612 open?id=13Y2XRT\\_ubNTCzvi6uIJbc\\_\\_iT6O6XQ90](https://drive.google.com/open?id=13Y2XRT_ubNTCzvi6uIJbc__iT6O6XQ90)
- 1613 van Zelst I, Wollherr S, Gabriel AA, Madden E, van Dinther  
1614 Y (2019) Modelling coupled subduction and earthquake  
1615 dynamics. DOI 10.31223/osf.io/f6ng5, URL [eartharxiv.org/  
1616 f6ng5](https://eartharxiv.org/f6ng5)

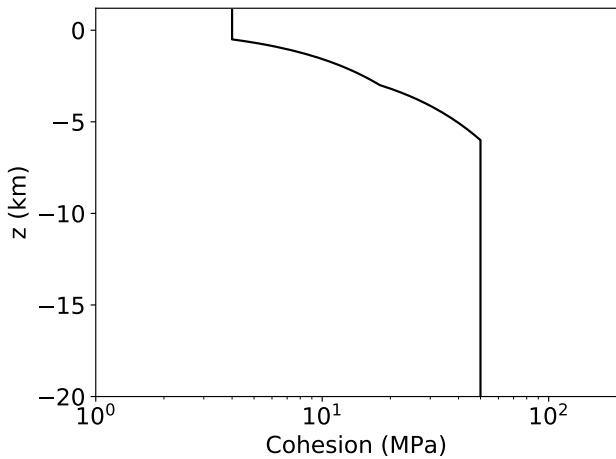


**Fig. S1** Depth dependence of cohesion in the off-fault plastic yielding criterion

## 8 Appendix

### 8.1 Off-fault plasticity

We account for the possibility of off-fault energy dissipation, by assuming a Drucker-Prager elasto-viscoplastic rheology (Wollherr et al, 2018b). The model is parameterized similarly as in Ulrich et al (2019). The internal friction coefficient is set equal to the reference fault friction coefficient (0.6). Similarly, off-fault initial stresses are set equal to the depth-dependent initial stresses prescribed on the fault. The relaxation time  $T_r$  is set at 0.05 s. Finally, the cohesion is assumed depth dependent (see Fig. S1) to account for the tightening of the rock structure with depth.

### 8.2 Displacement time histories

Many high-rate GNSS stations have recorded the Palu event in the near field (Simons et al, 2018). Nevertheless, these data are not yet available. In Figure S2, we provide the displacements time histories at a few of these sites. We hope future access to this data will provide further constraints to our model.

### 8.3 Initial stress

In this section, we detail the initial stress parametrization, presented in general terms in 3.2.

The fault system is loaded by a laterally homogeneous regional stress regime. Assuming an Andersonian stress regime, where  $s_1 > s_2 > s_3$  are the principal stresses and  $s_2$  is vertically oriented, the stress state is fully characterized by four parameters:  $SH_{\max}$ ,  $\nu$ ,  $R_0$

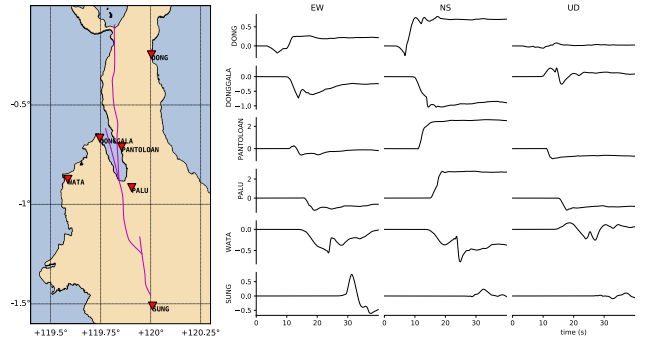


**Fig. S2** (a) Locations of known geodetic observation sites for which we provide synthetic ground displacement time series. (b) Synthetic unfiltered time-dependent ground displacement in meters at selected locations.

and  $\gamma$ .  $SH_{\max}$  is the azimuth of the maximum horizontal compressive stress;  $\nu$  is a stress shape ratio balancing the principal stress amplitudes;  $R_0$  is a ratio describing the relative strength of the faults; and  $\gamma$  is encapsulating fluid pressure.

The World Stress Map (Heidbach et al, 2018) constrains  $SH_{\max}$  to the range of  $120 \pm 15^\circ$ . The stress shape ratio  $\nu = (s_2 - s_3)/(s_1 - s_2)$  allows characterizing the stress regime:  $\nu \approx 0.5$  indicates pure strike-slip,  $\nu > 0.5$  indicates transtension and  $\nu < 0.5$  indicates transpression. A transtensional regime is suggested by geodetic studies (Walpersdorf et al, 1998; Socquet et al, 2006), fault kinematic analyses from field data (Bellier et al, 2006), and by the USGS focal mechanism of the mainshock, which clearly features a normal faulting component. However, the exact value of  $\nu$  is not constrained.

The fault prestress ratio  $R_0$  describes the closeness to failure of a virtual, optimally oriented plane according to Mohr-Coulomb theory (Aochi and Madariaga, 2003). On this virtual plane, the Coulomb stress is maximized. Optimally oriented planes are critically loaded when  $R_0 = 1$ . Faults are typically not optimally oriented in reality. In a dynamic rupture scenario, only a small part of the modeled faults need to reach failure in order to nucleate sustained rupture. Other parts of the fault network can break cascadingly even if well below failure before rupture. The propagating rupture front raises the local shear tractions to match fault strength locally.

We assume fluid pressure  $\gamma$  throughout the crust is proportional to the lithostatic stress:  $P_f = \gamma \sigma_c$ , where  $\gamma$  is the fluid-pressure ratio and  $\sigma_c = \rho g z$  is the lithostatic pressure. A fluid pressure of  $\gamma = \rho_{\text{water}}/\rho = 0.37$  indicates purely hydrostatic pressure. Higher values correspond to overpressurized stress states. Together,  $R_0$

and  $\gamma$  control the average stress drop  $d\tau$  in the dynamic rupture model as:

$$d\tau \sim (\mu_s - \mu_d)R_0(1 - \gamma)\sigma_c. \quad (2)$$

The such prescribed average stress drop  $d\tau$  is a critical characteristic of our model, controlling the average fault slip, rupture speed and rupture size.

Following Ulrich et al (2019), we can evaluate different stress and strength initial settings using purely static considerations. By varying the stress parameters within their observational constrains we compute the distribution of the relative prestress ratio  $R$  and of the shear traction orientation resolved on the fault system for each configuration.  $R$  is defined by:

$$R = (\tau_0 - \mu_s\sigma_n)/((\mu_s - \mu_d)\sigma_n), \quad (3)$$

where  $\tau_0$  and  $\sigma_n$  are the initial shear and normal tractions resolved on the fault plane and  $\mu_s$  and  $\mu_d$  are the static and dynamic fault friction assigned in the model.

We can characterize the spatially variable fault strength in our model by calculating  $R$  (Eq. (3)) at every point on each fault (Fig. S3 and S4). By definition,  $R$  is always lower or equal to  $R_0$ , since the faults are not necessary optimally oriented.

We then select the stress configuration that maximizes  $R$  across the fault system, especially around rupture transition zones to enable triggering, and that represents a shear stress orientation compatible with the inferred ground deformations and the inferred focal mechanisms.

Our purely static considerations suggest that a trans-tensional regime is required to achieve a favourable stress orientation on the fault system. In fact, we see that a biaxial stress regime ( $\nu = 0.5$ ) does not resolve sufficient shear stress simultaneously on the main north-south striking faults and on the Palu-Saluki bend (see Fig. S3). Dynamic rupture experiments confirm that the Saluki fault could not be triggered under such a stress regime. On the other hand, such optimal configuration can be achieved by a transtensional stress state, for instance by choosing  $\nu = 0.7$  and  $SH_{\max}$  in the range  $125$  to  $135^\circ$  (see fig. S4). We choose  $SH_{\max} = 135^\circ$ , which allows for nucleation with less overstress than lower values and generates ruptures with the expected slip orientations and magnitudes.

The here assumed fault system does not feature pronounced geometrical barriers apart from the Palu-Saluki bend. As a consequence,  $R_0$  is actually poorly constrained, and trade-offs between  $R_0$  and  $\gamma$  are expected. The preferred, realistic model is characterized by  $R_0 = 0.7$  and  $\gamma = 0.79$ . This results in an effective confining stress  $(1 - \gamma)\sigma_c$  that increases with depth by a gradient of  $5.5$  MPa/km.

**Table S1** Fault frictional properties assumed in this study.

Direct-effect parameter	a	0.01
Evolution-effect parameter	b	0.014
Reference slip rate	$V_0$	$10^{-6}$ m/s
Steady-state low-velocity friction coefficient at slip rate $V_0$	$f_0$	0.6
Characteristic slip distance of state evolution	L	0.2 m
Weakening slip rate	$V_w$	0.1 m/s
Fully weakened friction coefficient	$f_w$	0.1
Initial slip rate	$V_{\text{ini}}$	$10^{-16}$ m/s

#### 8.4 Friction law

We here use a form of fast-velocity weakening friction proposed in the community benchmark problem TPV104 of the Southern California Earthquake Center (Harris et al, 2018) and as parameterized by Ulrich et al (2019). Friction drops rapidly from a steady-state, low-velocity friction coefficient, here  $f_0 = 0.6$ , to a fully weakened friction coefficient, here  $f_w = 0.1$  (see Table S1).

#### 8.5 Horizontal displacements as additional tsunami source

For computing the seafloor displacement used as source for the tsunami model, we apply the method of Tanioka and Satake (1996) to additionally account for horizontal displacements, computed from the earthquake simulation. The final states of the three components  $\Delta x, \Delta y$  and  $\Delta z$  are given in Fig. S5. Applying the approach of Tanioka and Satake by using Eq. (1) the vertical displacement translates into  $\Delta b$ , which is given in Fig. 7. The difference between  $\Delta z$  and  $\Delta b$  locally amounts up to  $0.6$ m as shown in Fig. S6. Although this difference is quite remarkable and compared to the overall magnitude more than  $30\%$ , it is only very local. Due to the local bathymetry of Palu bay it also not only amplifies the displacement, but also diminishes it at some locations.

The local influence of the method by Tanioka and Satake (1996) can be seen by comparison to the results section. We have run a similar simulation as described in the main part of the paper, but with the computed seafloor displacement  $\Delta z$  as source for the tsunami model. Snapshots of this scenario in Palu Bay can be seen in Fig. S7. Compared to the original scenario (cf. Fig. 9) only local effects are visible, especially at points along the coast. The maximum inundation at Palu city is given for this alternative scenario in Fig. S8. Again, only minor differences appear compared to the

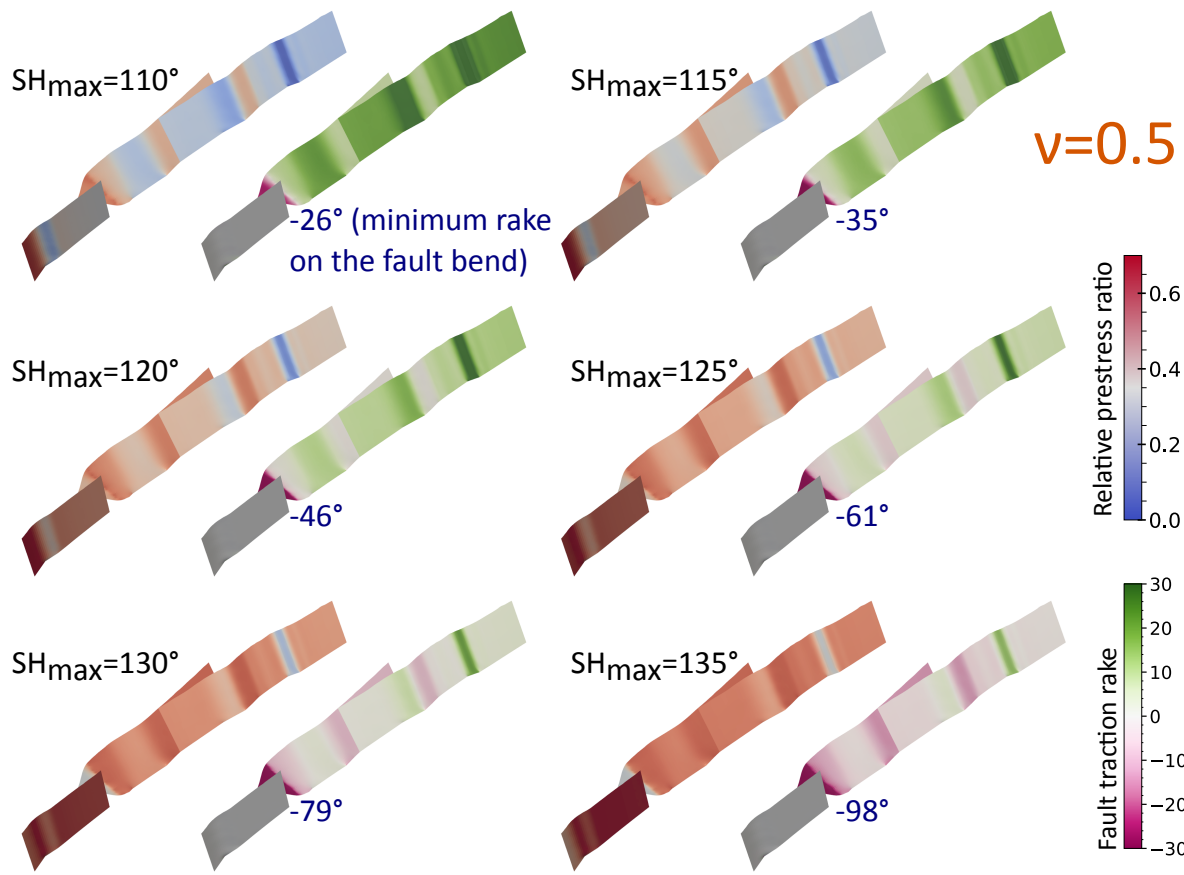


**Fig. S3** Magnitude and rake of prestress resolved on the fault system for a range of plausible  $SH_{\max}$  values, assuming a stress shape ratio  $\nu = 0.5$  (pure-shear). For each stress state, we show the spatial distribution of the pre-stress ratio (left) and the rake angle of the shear traction (right). Here we assume  $R_0 = 0.7$  on the optimal plane, which results in  $R < R_0$  for all faults since these are not optimally oriented. In blue, we label the (out-of-scale) minimum rake angle on the Palu-Saluki bend.

1766 computation which includes horizontal displacements in  
 1767 the source (cf. Fig. 13). This illustrates that the method  
 1768 by Tanioka and Satake (1996) might be important to  
 1769 capture some local effects of the tsunami, but is not  
 1770 crucial for the general result, which is also confirmed by  
 1771 other studies (Heidarzadeh et al, 2018).

ing, 2017; Rosen et al, 2012) for ALOS-2 SAR data  
 processing.

1783  
 1784

## 1772 8.6 Along-track SAR measurements

1773 We here describe our measurements of the final coseismic  
 1774 surface displacements in along-track direction from SAR  
 1775 images acquired by the Japan Aerospace Exploration  
 1776 Agency (JAXA) Advanced Land Observation Satellite-2  
 1777 (ALOS-2) SAR. We measure along-track pixel offsets  
 1778 incoherent cross correlation of ALOS-2 stripmap SAR  
 1779 images acquired along ascending path 126 on 2018/08/17  
 1780 and 2018/10/12 and ascending path 127 on 2018/08/08  
 1781 and 2018/10/03. We used modules of the InSAR Scientific  
 1782 Computing Environment (ISCE) (Liang and Field-



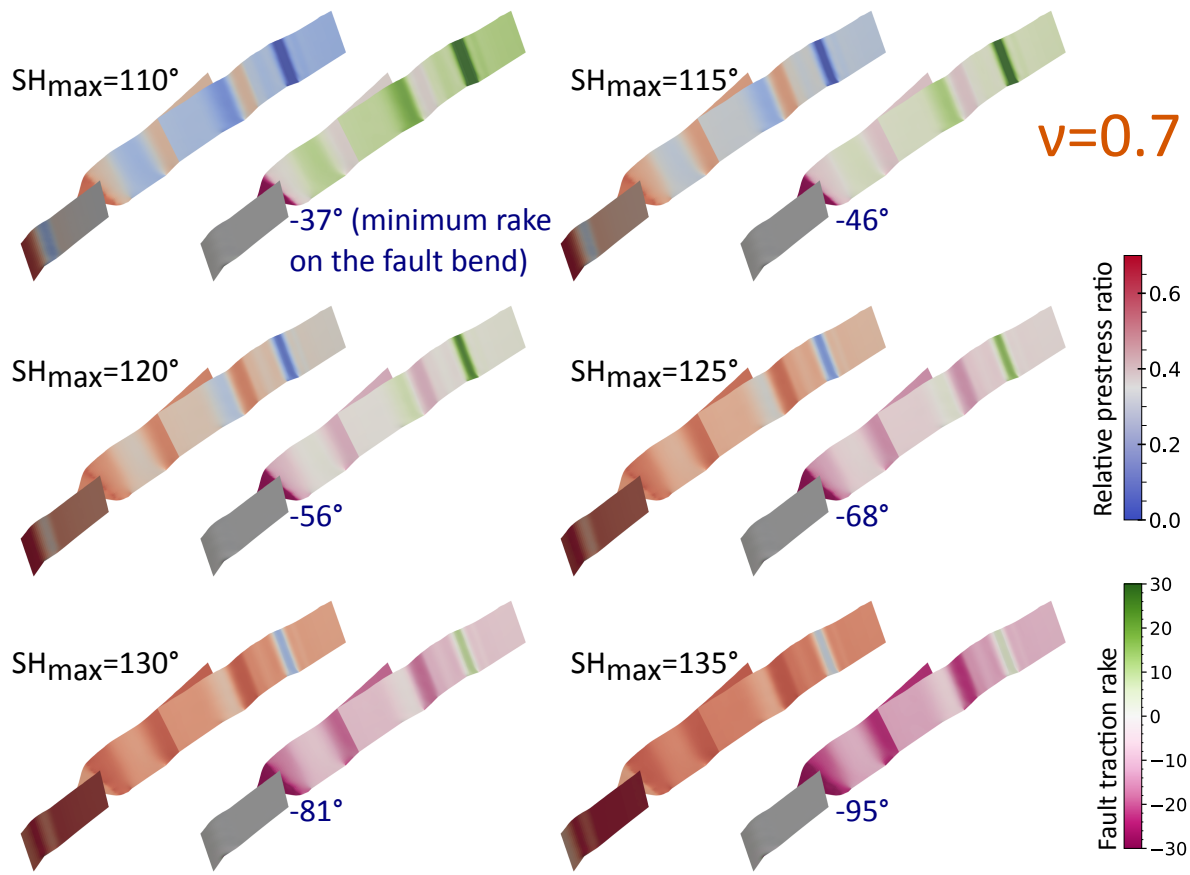


**Fig. S4** Same as Fig. S3, but assuming a stress shape ratio  $\nu = 0.7$  (transtension).

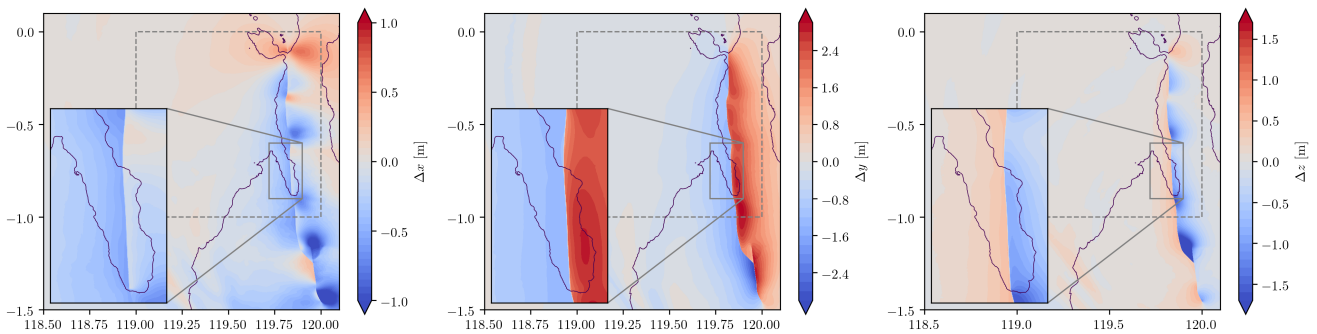


**Fig. S5** Final horizontal ( $\Delta x$  and  $\Delta y$ ) and vertical ( $\Delta z$ ) surface displacements as computed by the earthquake model.

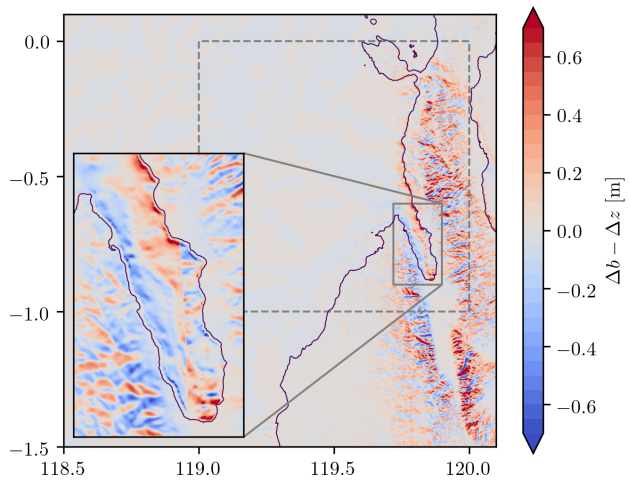


**Fig. S6** The contribution  $\Delta b - \Delta z$  of horizontal displacements to the final bathymetry perturbation, following Tanioka and Satake (1996)

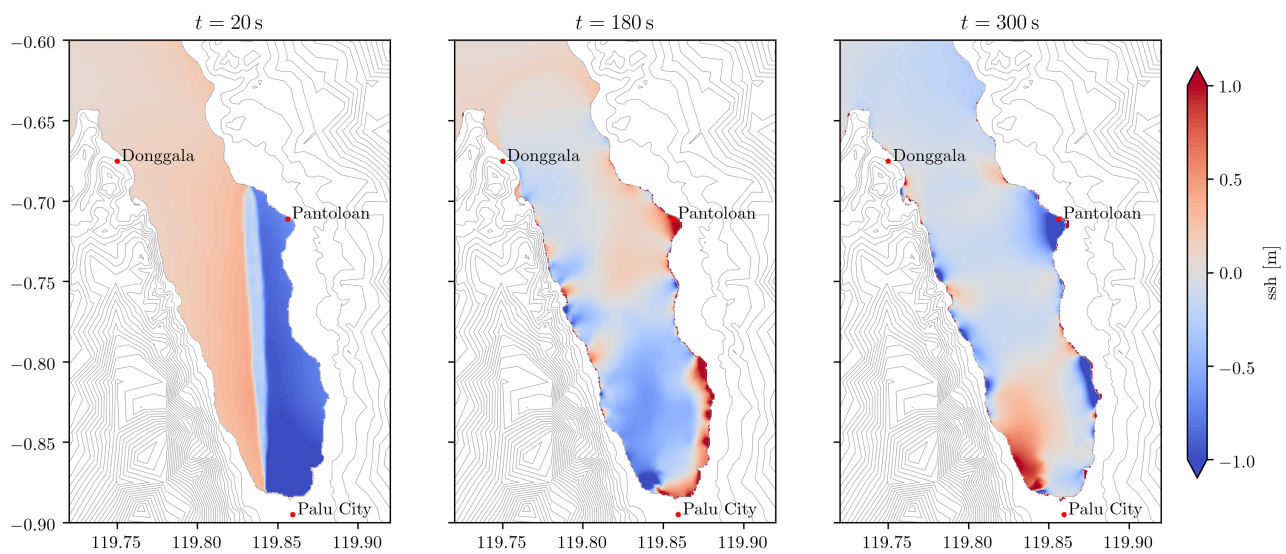


**Fig. S7** Snapshots at 20 s, 180 s, and 300 s of the tsunami scenario using only the vertical displacement  $\Delta z$  from the rupture simulation as source for the tsunami model.

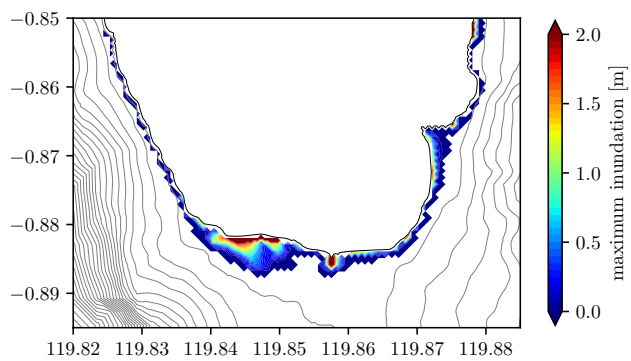


**Fig. S8** Computed maximum inundation at Palu City using only the vertical displacement  $\Delta z$  from the rupture simulation as source for the tsunami model.